EMBEDDED POWER MANAGEMENT AND CONTROL FOR HARVESTED ENERGY

A Dissertation

Presented to the Faculty of the Graduate School

of Cornell University

in Partial Fulfillment of the Requirements for the Degree of

Doctor of Philosophy

by

Alexander Douglas Schlichting

January 2014

EMBEDDED POWER MANAGEMENT AND CONTROL FOR HARVESTED ENERGY

Alexander Douglas Schlichting, Ph.D.

Cornell University 2014

Small-scale, low-mass embedded systems have received significant interest in a variety of applications as the capabilities of embedded electronics have increased. Examples of new realizable applications are self-reliant bio-loggers and tracking tags for small animals. Due to the small scale and low power levels, the power management for these systems presents significant challenges. In this dissertation, research will be presented on various aspects of the flow of energy on a self-reliant embedded system. First, an investigation into the dynamics of combining the power from multiple energy harvesting devices will be shown. The work provides guidelines for energy harvesting systems combining photovoltaic and piezoelectric devices as well as an array of multiple piezoelectric devices. Using the knowledge gained from this work, effective multi-source energy harvesting systems can be designed. Next, a novel method for the low-loss AC-DC rectification of a vibration energy harvester is presented and evaluated. The new rectification technique allows for more efficient power conversion in addition to the rectification of low-voltage harvesting systems. This is performed without active electrical circuitry and does not require external power sources for full operation. The last topic is the investigation of the energy storage design challenges for a self-reliant avian bio-logger. Prototypical operation requirements are developed to determine the most pertinent challenges and a preliminary system design is presented and evaluated. Using

the analyses performed on the prototypical system, new small-scale self-reliant embedded systems can be realized to further increase the tools scientists have at their disposal for understanding the behavior of small animals.

BIOGRAPHICAL SKETCH

Alex Schlichting grew up in Arlington, Virginia. He attended Washington-Lee High School and earned an International Baccalaureate Diploma in addition to his high school diploma. He then went on to study Mechanical Engineering at Carnegie Mellon University in Pittsburgh, Pennsylvania due to his passion for science and problem solving. He completed a Bachelor's of Science in the spring of 2009. During his time at Carnegie Mellon he played on the water polo club, being elected team president his junior and senior years. He also is a member of Sigma Nu fraternity. He was elected to numerous positions while at Carnegie Mellon, culminating as the treasurer on the executive board. As part of Sigma Nu, he participated in Carnegie Mellon's Sweepstakes athletic and engineering competition. He served as an A-team athlete (pusher) all four years in addition to helping design and build a new competition vehicle (buggy).

During his undergraduate studies, Alex had multiple research-oriented internships and projects. The summer before his junior year, he participated in the National Science Foundation Research Experiences for Undergraduates program at Virginia Polytechnic Institute and State University. His project was in the Center for Intelligent Material Systems and Structures under the guidance of Prof. Daniel J. Inman and Steven Anton. It is during this internship where Alex 'caught the Ph.D. bug'. The following summer he participated in the National Aeronautics and Space Administration's Undergraduate Student Research Program at the Glenn Research Center. His mentors were Andrew Provenza, Jeffery Trudell, and Dr. Kirsten Duffy. Alex also did a College of Engineering Senior Honors Research Project with Prof. O. Burak Ozdoganlar and Prashanth Anandan in the Multiscale Manufacturing and Dynamics Laboratory at Carnegie Mellon University. During his last summer before starting

his graduate school studies, Alex had an internship as part of the Dynamics Summer School in the Los Alamos National Laboratory's Engineering Institute under the direction of Dr. Charles Farrar. His mentors for the research project were Dr. Kevin Farinholt and Dr. Gyuhae Park and his groupmates were Scott Ouellette and Clinton Carlson.

Alex started the Ph.D. program in the Sibley School of Mechanical and Aerospace Engineering in the fall of 2009. He immediately started working with Prof. Ephrahim Garcia, whom he sought out before even applying due to his work in the field of smart materials and on the advice of Prof. Garcia's own Ph.D. advisor, Prof. Daniel J. Inman. Alex worked on multiple different projects for various sponsors. He also served as a laboratory teaching assistant for the department three times. Although he initially focused on energy harvesting and started exploring multi-source systems almost immediately, his focus broadened and caused him to explore small-scale, low-power embedded systems as part of his Electrical Engineering minor. This new focus culminated with the Digital System Design: Microcontrollers course taught by Dr. Bruce Land. At the end of his Ph.D. program, Alex has a first-author journal article published in *Smart Materials and Structures* and another in the *Journal of Intelligent Material Systems and Structures*. He has one more first-author journal article submitted to *Smart Materials and Structures*.

This dissertation is dedicated to all of those who have helped me get to where I am. First are my parents, who realized my brother and I were going to be significantly more technical than them the moment we started building cranes and solid brick ships out of LEGOS®. I will always be thankful that you could not wait for me to get my driver's license so I could get myself around as opposed to being worried I was out on my own. Then there is my brother, who I did everything with until he went to college (figuratively speaking). I also will never forget my neighbors Bill and Kay Plitt, who still tell me they will always be my biggest fans.

Now come a bunch of sweeping statements as there are too many of you to list and thank individually. First are the violin teachers and orchestra conductors who helped me realize my creative potential and taught me the value of diligent practice and hard work. Next, the sports coaches who never did get to see me finally grow into my lanky frame (if it has happened yet) and always understood that I was a scholar first. Then of course all the teachers and professors who graded me harder (of course my mother colluded on this one) or drove me to press my limits and boundaries. Last but not least, my Ph.D. advisor E, who always thought I needed more caffeine.

This last paragraph I save for the friends and colleagues at every step along the way who have helped me in a multitude of ways. Whether it was being there when I needed support, or just needed to let loose and have fun, your help is always appreciated and never forgotten.

ACKNOWLEDGEMENTS

The author would like to acknowledge the co-authors on the chapters of his dissertation: Prof. Ephrahim Garcia, Dr. Rashi Tiwari, and Ericka Fink. He would also like to acknowledge the contributions and help of Dr. Matthew Bryant, Dr. Bruce Land, Michael Shafer, and the rest of his Laboratory for Intelligent Machine Systems labmates and colleagues.

The first chapter of this work was performed with the guidance and support of Hyungjae Shim and the Samsung Synergistic Modalities for Energy Harvesting in Personal Electronics Project.

The second chapter of this work was performed with the support of both the National Science Foundation IDR 1014891: Self-Reliant Autonomous Microsystems for Biophysical Monitoring of Small Animals (Lab-on-a-Bird) and the NSF TANMS NERC under the Cooperative Agreement Award EEC-1160504.

The third chapter of this work was performed with the support of the National Science Foundation IDR 1014891: Self-Reliant Autonomous Microsystems for Biophysical Monitoring of Small Animals (Lab-on-a-Bird).

TABLE OF CONTENTS

LIST OF FIGURES

LIST OF TABLES

LIST OF ABBREVIATIONS

For Chapter 1:

DC Direct current
AC Alternating current
$MPPT$ Maximum power point tracking
PZT lead zirconate titanate
S Single solar energy harvester
P Single piezoelectric energy harvester
SPS Solar and piezoelectric harvesters in series topology
SPP Solar and piezoelectric harvesters in parallel topology
PPS Two piezoelectric harvesters in series topology
PPP Two piezoelectric harvesters in parallel topology

For Chapter 2:

RMS Root mean squared

For Chapter 3:

MCU Microcontroller
GPS Global positioning system
TX Wireless transmission mode
RX Wireless receiving mode
SOC Battery state of charge
$VRLA$ Valve-regulated lead-acid battery

LIST OF SYMBOLS

For Chapter 1:

C_L Storage capacitor for all topologies
Z_C Thévenin model equivalent impedance
I_L Photovoltaic photogenerated current
I_S Photovoltaic pn-junction saturation current
q Charge in an electron
T Photovoltaic pn-junction temperature
k Boltzmann constant
n Photovoltaic pn-junction diode emissivity
f Frequency
A Amplitude
ϕ Phase
V_{CL} Voltage of the storage capacitor
E_{CL} Energy in the storage capacitor
P_{CL} Instantaneous power of the storage capacitor
P_{avg} Average power
r Ratio of maximum solar power to piezoelectric power

For Chapter 2:

V_F/V_γ Semiconductor diode forward voltage drop
I_F Semiconductor diode forward current
V_P Piezoelectric voltage
C_S Smoothing capacitance
R_L Load resistance
V_R Semiconductor diode reverse blocking voltage
I_R Semiconductor diode reverse leakage current
$V_{R,max}$ Maximum semiconductor diode reverse blocking voltage
R_C Reed switch contact resistance
t_O Reed switch operation time (including bouncing due to contact)
t_R Reed switch release time
l Reed switch enclosure length
d Reed switch enclosure diameter

SW_P Reed switch pair

V_{ideal} Ideal AC-DC full-bridge rectifier output voltage

A Ideal output voltage amplitude

V_{offset} Semiconductor diode model AC-DC full-bridge rectifier output voltage

V_{reed} Reed switch AC-DC full-bridge rectifier output voltage

t_{delay} Reed switch rectification proximity delay for oscillation half period

t_{open} Reed switch open time for oscillation half period

n_{hyst} The magnetic hysteresis of the reed switch and magnet pair

V_{hybrid} Hybrid AC-DC full-bridge rectifier output voltage

For Chapter 3:

V_{OC} Maximum battery open circuit voltage

$R_{Int.}$ Battery internal series resistance

I_{max} Maximum battery discharge current

V_{BATT} Battery terminal voltage

P_{BATT} Battery power (discharge positive)

CHAPTER 1

PASSIVE MULTI-SOURCE ENERGY HARVESTING SCHEMES [1]

1.1 Introduction

As electronic systems decrease in size and become more mobile, power source endurance becomes increasingly important. As a power source's energy capacity is proportional to its mass and volume, there is a trade-off between endurance and size. One approach to this issue is to recharge the batteries without plugging into an existing power grid. This involves storing energy gathered from the environment using transducers, also known as energy harvesting. There are many desirable applications of energy harvesting, such as wireless sensor networks [51, 49, 46], wildlife tracking [40], and personal electronics like cell phones. Significant amounts of work has explored the geometric optimization of energy harvesting devices [18]. As a result, research has shifted to using complex feedback control circuitry, among other topics.

Many of the schemes focus on power maximization from the harvester [76, 11, 36, 74, 34, 27, 28, 63, 37, 38, 32]. While the schemes produce significant increases in the maximum instantaneous power produced, they all draw from the stored energy to control the additional circuitry. Guan and Liao (2007) investigates the harvesting efficiency of the Impedance Adaptation method [48] as compared to a passive harvesting circuit with only a full-bridge rectifier. The results show that the passive method is more efficient at harvesting and storing energy due to the power losses in the components needed for the Impedance

[1] This chapter was originally published as a journal article in the *Journal of Intelligent Material Systems and Structures* [57] and is reproduced here with permission of SAGE Publications.

Adaptation method. Also, most of the methods make use of inductors to minimize the power losses resulting from the associated switching. As the inductor voltage decreases, the efficiency of the inductor decreases and the size increases. Therefore, with low-voltage harvesters, these methods result in unfavorable trade-offs between performance and mass [12]. Others focus on the overall power management of the system as well [31, 47]. Regardless of the method, more applications and opportunities for energy harvesting can be realized by increasing the power output of the harvesting system.

Another method for increasing the robustness and versatility of energy harvesting systems is to utilize multiple harvesters simultaneously [40, 39, 73, 49, 46]. The idea of combining multiple systems for stand-alone power generation onto one energy storage unit first appeared with large-scale power generation systems [72, 71, 41, 20, 17, 4]. While these studies focused on stand-alone power generation systems for residential applications, energy harvesting applications present different challenges in terms of power levels, size and mass. The lower power levels available emphasize the need for a very efficient power management system. Figure 1.1 illustrates the flow of power in a multi-source system from the different harvesters, through the conditioning circuitry into the energy storage medium, and then to the load. The energy harvesters shown represent the most commonly used methods: piezoelectric and photovoltaic. Any power lost to the control of the conditioning circuitry or for the transfer of power is represented.

Initial prototypes of adaptive, multi-source energy harvesting systems exist in the literature [49, 46]. They use active control systems to isolate the harvesters and combine the energy onto a single power source for wireless sensor nodes.

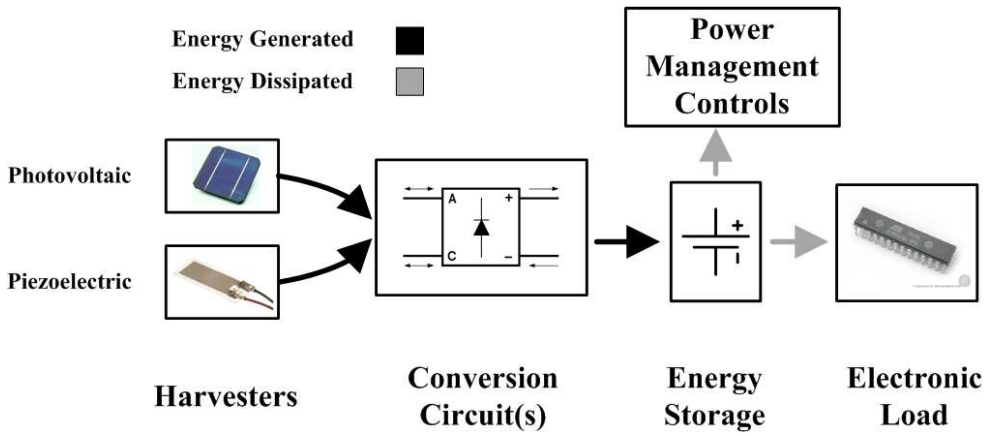

Figure 1.1: Multi-source energy harvesting schematic

Park and Chou (2006) combine solar and wind energy onto a lithium-polymer battery using a supercapacitor array charged through DC-DC boost regulators by the harvesters. The DC-DC boost regulators are part of a closed-loop maximum power point tracking (MPPT) technique to transfer power to the capacitors. This system uses only analog components for the control and consumes less than 1.65 mW. Morais et al. (2008) charge a nickel-metal hydride battery with a solar cell, a wind generator and a hydroelectric turbine. The energy on separate buffer capacitors is transferred to the battery using DC-DC boost converters as switches, which are controlled using a microcontroller.

This work explores passive multi-source energy harvesting schemes for combining power from multiple harvesters onto a single storage capacitor. These schemes do not suffer from additional power losses or complexity from active switching power management systems and can be used as a baseline for comparison with more complex methods. Also, due to the passive nature of the schemes they do not need to be designed or adjusted to the excitation frequency. This attribute makes them a practical comparison for baseline purposes and an option for stochastic or widely varying excitation frequencies. Two cases are

explored: one using a piezoelectric and a photovoltaic harvester and the other using an array of piezoelectric harvesters. Both series and parallel topologies are considered. Circuit simulations (LTspice IV) provide a fast and repeatable method for characterizing the dynamics of these circuit topologies while using accepted piezoelectric and photovoltaic circuit models. The results and techniques presented should not be thought limited to the aeroelastic energy harvesters or the solar cells reported, but the circuits applicable to any multi-source energy harvesting system using either a piezoelectric and a solar harvester or an array of piezoelectric harvesters.

1.2 Multi-source schemes analysis

This section explains the methods used to analyze the results of the simulations. The maximum instantaneous power flow is used to evaluate the capabilities of the harvester when it's operating at its peak performance levels. Power here refers to the instantaneous power of the storage capacitor, P_{CL}, (equation (1.1)). Also, unless otherwise noted, the voltage, power, energy, and charge time variables all refer to the storage capacitor, C_L, for each topology. Since the piezoelectric harvester's signal is AC, much of the data oscillates at the rectified piezoelectric frequency of $2 \times f_P = 10$ Hz. Connecting the maximums or minimums of each oscillation cycle creates smoothed data sets which represent the upper or lower envelopes of the data, respectively. Viewing the data in this manner allowed for a clearer interpretation of the behavior of the system by eliminating the 10 Hz oscillation from the plots. Figure 1.2 shows the upper envelope of an

example set of data.

$$P_{CL}(t) = V_{CL}(t)\, I_{CL}(t) = \left(C_L \dot{V}_{CL}(t)\right) V_{CL}(t) \tag{1.1}$$

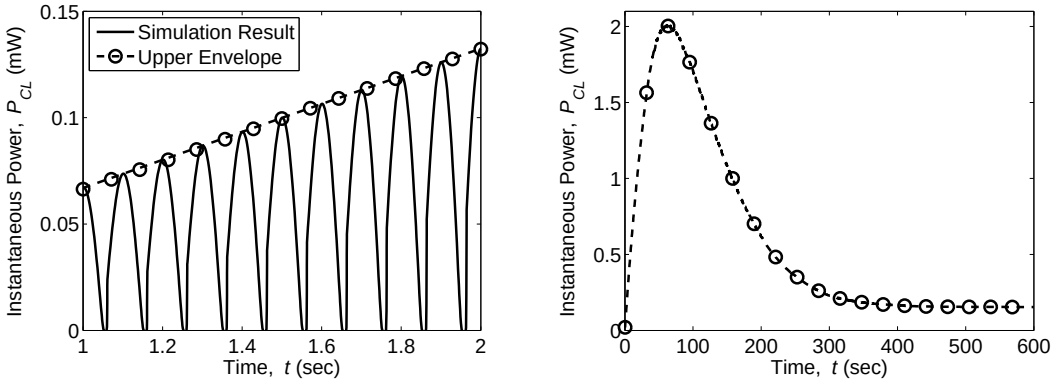

(a) (b)

Figure 1.2: Example of the creation (a) and result (b) of the storage capacitor power upper envelope

Average power,P_{avg} (equation (1.2)), calculations examined the effectiveness of the topology at storing the harvested energy over the entire charge cycle. The charging time, t_f, is defined as the time it took for the capacitor voltage to be within 2% of its final value for the multi-source topology being analyzed. The initial time, t_o, represents the start of the charging cycle, or zero in this case. Examining the average power avoids dealing with the dependence of the energy level and charge time metrics on the storage capacitance during the analysis.

$$P_{avg} = \frac{1}{t_f - t_o} \int_{t_o}^{t_f} P_{CL}(t)\, dt \tag{1.2}$$

1.2.1 Piezoelectric circuit model

The Thévenin equivalent circuit model shown in figure 1.3b exhibits the same impedance behavior as lead zirconate titanate (PZT) [50]. It represents the

piezoelectric cantilever harvester shown in figure 1.3a for systems with low electromechanical coupling. This model is built on many assumptions, such as that the beam is always excited at resonance and that the excitation amplitude is constant. Wickenheiser et al. (2010a) experimentally proved that the assumption of constant excitation amplitude is valid for piezoelectric energy harvesters with low electromechanical coupling. Harvesters with low electromechanical coupling are preferable for the low-amplitude vibration sources commonly seen in desired energy harvesting applications. The simulations reported herein use the ideal Thévenin equivalent circuit with $Z_C = C_P$.

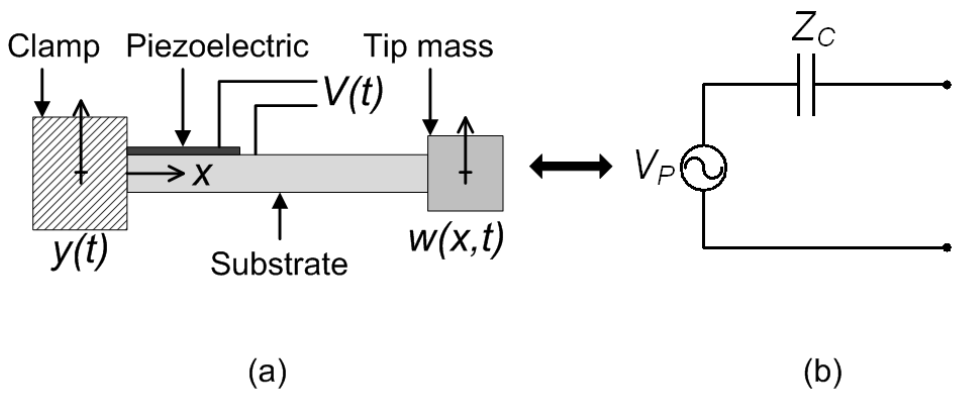

Figure 1.3: The (a) standard physical piezoelectric energy harvester and the (b) Thévenin piezoelectric equivalent circuit

The aforementioned aeroelastic flutter wind energy harvester served as the baseline for the piezoelectric circuit model. A pair of MIDE Quickpack QP10n piezoelectric patches is adhered to base of the beam in a bimorph configuration [7]. Unless otherwise stated, the simulation parameters are: $A_P = 30$ V, $f_P = 5$ Hz, and $C_P = 110$ nF, to match the experimentally obtained 2 mW maximum power output of the aeroelastic flutter wind energy harvesters across a 263 kΩ load. Here, A_P represents the amplitude of the AC piezoelectric voltage signal

and f_P the oscillation frequency. This wind energy harvester was chosen due to its high voltage level, an oscillation frequency in the range of many environmental vibration sources, and its low electromechanical coupling. Figure 1.4 shows the typical piezoelectric energy harvesting circuit used with a storage capacitor and a full-bridge rectifier. For the simulations, the LTspice model for the On Semiconductor MBR0520L Schottky diodes was used to reduce the effects of diode voltage drops. The model for the TDK C575OX5ROJI07M, 100 μF storage capacitor was chosen to sufficiently reduce the ripple in the rectified signal.

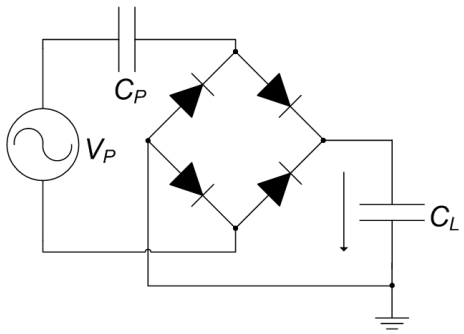

Figure 1.4: Separate piezoelectric charging circuit P

1.2.2 Photovoltaic circuit model

The photovoltaic circuit model assumes an ideal cell, with ideal I-V characteristics (figure 1.5) [67]. It is comprised of a constant current source, I_L, in parallel with a diode, D_{PV}. Here, I_L represents the photogenerated current and D_{PV} the pn-junction of the cell. The current output of the photovoltaic cell is defined by equation (1.3), where I_S is the diode saturation current, q is the charge of an electron, T is the diode temperature, and k is Boltzmann's constant.

$$I = I_L - I_S \left(e^{\frac{qV}{kT}} - 1 \right) \tag{1.3}$$

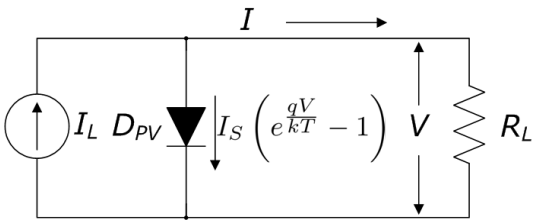

Figure 1.5: Ideal photovoltaic cell circuit model

To create the model for the diode, the emission coefficient, n, is inserted into the junction current equation as per the Shockley ideal diode equation (equation (1.4)). Here, $I_{D,\,PV}$ is the pn-junction diode current. Rearranging to solve for the emission coefficient, as shown in equation (1.5), the diode model for the junction is defined by the saturation current and the emission coefficient. A constant solar radiation is assumed for the simulations reported herein. Therefore, the maximum specifications for current and voltage for the photovoltaic replaced the diode current and voltage ($I_{D,\,PV} = I_{PV,\,max}$ and $V_{D,\,PV} = V_{PV,\,max}$) as given in equation (1.6)[60].

$$I_{D,\,PV} = I_S\left(e^{\frac{qV_{D,\,PV}}{nkT}} - 1\right) \tag{1.4}$$

$$ln\left(\frac{I_{D,\,PV}}{I_S} + 1\right) = \frac{qV_{D,\,PV}}{nkT} \;\Rightarrow\; n = \frac{qV_{D,\,PV}}{ln\left(\frac{I_{D,\,PV}}{I_S} + 1\right)kT} \tag{1.5}$$

$$n \approx \frac{qV_{PV,\,max}}{ln\left(\frac{I_{PV,\,max}}{I_S}\right)kT} \quad , \qquad \text{for } I_{PV,\,max} \gg I_S \tag{1.6}$$

For the photovoltaic harvesters, a thin film panel from Silicon Solar, Inc., served as the baseline for the photovoltaic model: $V_{PV,\,max} = 6$ V and $I_{PV,\,max} = 50$ mA. To produce theoretical maximum power outputs other than 300 mW, $I_{PV,\,max}$ varies while $V_{PV,\,max}$ stays constant. A 10 pA saturation current and

room temperature ($T = 300\ K$) are assumed. To protect the photovoltaic, two diodes separate it from the storage capacitor, as shown in figure 1.6. The first diode, D, an ON Semiconductor 1N5819 Schottky diode model, prevents current from flowing from the storage capacitor into the photovoltaic. The second diode, D_Z, an ON Semiconductor BZX84C6V2L Zener diode model, limits the voltage over the solar cell to below the maximum 6 V specified by the manufacturers. Since the simulations use an ideal photovoltaic model there is no impedance for the harvester and the maximum power level does not vary with the load capacitance.

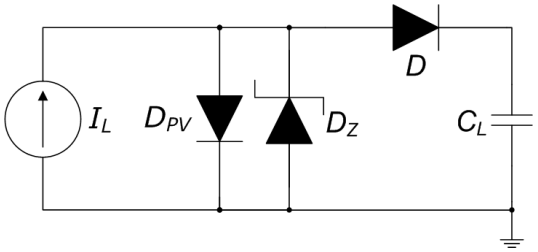

Figure 1.6: Photovoltaic charging circuit, S

1.2.3 Multi-source: solar & piezo

For this section, the addition of a subscript P denotes the piezoelectric harvester only, an S the solar harvester only, SPS the solar and piezoelectric harvesters in the series topology, and SPP the solar and piezoelectric harvesters in the parallel topology. Solar harvesters possess a much higher energy density than piezoelectrics and are commonly the first method considered, therefore the results in this section are presented as changes with regard to a solar harvester. Also, r (equation (1.7)) gives the ratio of the solar harvester output power to the peizoelectric's. When r varies, the solar harvester's output power is varies and

the piezoelectric power output remains constant.

$$r = \frac{P_{S,\,max}}{P_{P,\,max}} \tag{1.7}$$

Solar and piezo - series SPS topology

The rectified piezoelectric harvester is placed in series with the solar harvester (figure 1.7). The Zener diode, D_Z, prevents the voltage seen by the solar cell from exceeding its maximum allowable level of 6 V. These components are then placed in series with an ideal storage capacitor, C_L.

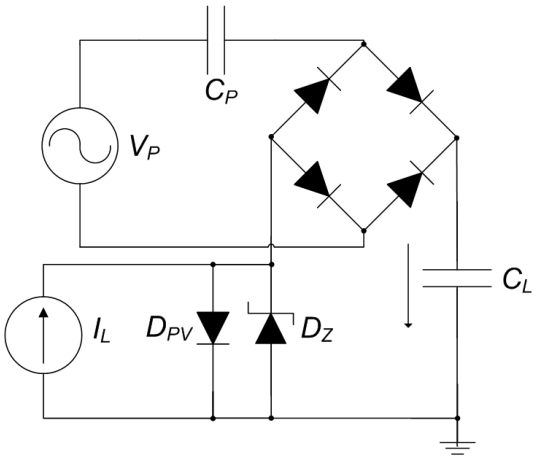

Figure 1.7: Passive solar and piezoelectric series topology, SPS

A significant advantage of the SPS topology is a higher available voltage. This is desirable for multiple reasons. First, the electronic components which the energy harvesting system typically power have a minimum voltage necessary to operate, normally around 2.2 to 3.6 V. As solar cells are low-voltage harvesters, the addition of a piezoelectric harvester can help meet these voltage requirements. Second, the higher the voltage, the more energy stored in the

capacitor for use by the electronic components (equation (1.8)).

$$E_{CL}(t) = \frac{1}{2} C_L V_{CL}(t)^2 \tag{1.8}$$

Solar and piezo - parallel SPP topology

The rectified piezoelectric harvester is placed in parallel with the solar harvester (figure 1.8). The Zener diode, D_Z, prevents the solar cell from seeing too high of a voltage just as in the SPS topology. The diode, D, prevents any backward current from flowing through the solar cell as it is no longer in the same current loop as the full-bridge rectifier. These components are placed in parallel with an ideal storage capacitor, C_L.

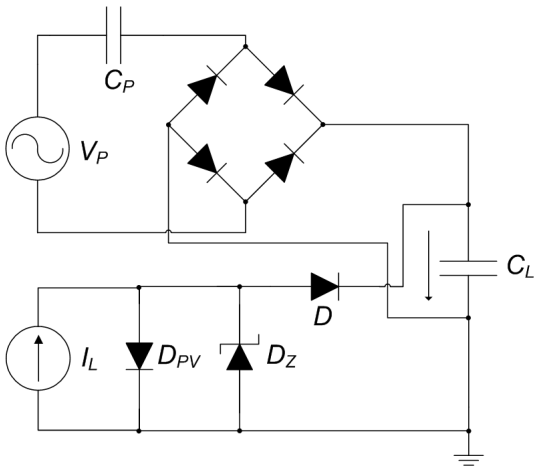

Figure 1.8: Passive solar and piezoelectric parallel topology, SPP

An advantage of the SPP topology is that the currents from the two systems are summed, not the voltage. For high-voltage harvesters, this topology would not result in significantly high voltages which could be more difficult to regulate to the 2.2 to 3.6 V range.

Solar and piezo - $r \approxeq 1$

One of the significant advantages of the SPS topology is that it allows for higher storage capacitor voltages and therefore higher amounts of stored energy. Figure 1.9 shows the storage capacitor energy curves during the charging cycles for both of the multi-source topologies as well as the separate piezo and solar harvesters. Due to the summation of the piezoelectric and solar voltage levels, the SPS topology's stored energy curve settles to a significantly higher value. The amount of energy stored due to the solar cell, shown in figure 1.9(b), is actually quite small in comparison to the other topologies. However, a caveat of the higher available voltages and stored energy is the amount of time it takes to charge up to the higher levels.

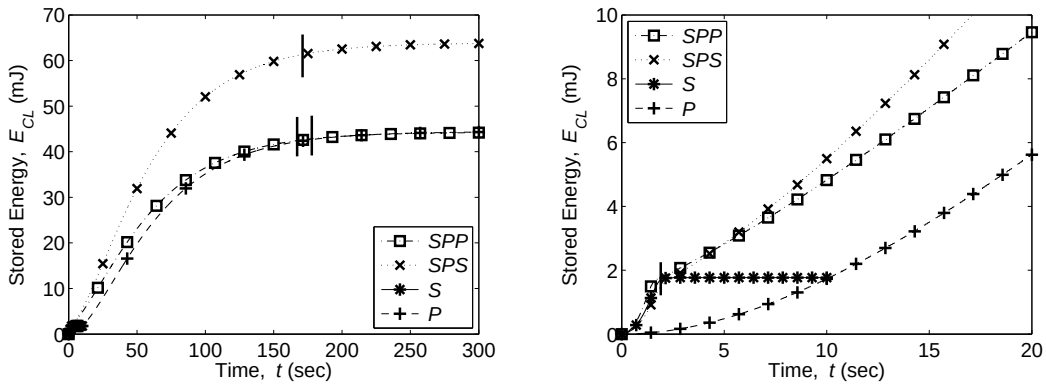

Figure 1.9: The capacitor stored energy curves for the SPS, SPP, P (a) and S (b) topologies with the charge times, t_f, marked

Examining the results shown in figure 1.9 as well as in table 1.1, the SPS topology stores approximately 37 times more energy than the solar cell, S. However, it takes approximately 90 times longer to store that energy. This relationship is represented much more cleanly by examining the average power of the energy charging cycles for the different topologies. Table 1.1 shows that the so-

lar harvester has an average power of 0.89 mW, while the SPS topology is only at 0.36 mW. The SPP topology's average power is lower, equal to that of the piezoelectric harvester, P, at 0.25 mW. The average power for the P topology is lower than that of the S topology even though $P_{P,\,max} \approxeq P_{S,\,max}$ because the oscillations of the rectified piezoelectric's AC signal prevent the steady flow of current into the capacitor that occurs with the solar harvester.

Table 1.1: Charging statistics for energy harvesting circuits

	S	P	SPS	SPP
Final voltage, V_f (V)	5.8	29	35	29
Final stored energy, E_f (mJ)	1.7	43	61	42
Charge time, t_f (sec)	1.9	178	171	167
Average power, P_{avg} (mW)	0.89	0.24	0.36	0.25
Maximum power, P_{max} (mW)	1.5	2.0	2.5	2.0

The addition of the piezoelectric to the solar harvester in either the SPS or SPP topology negatively affects the average power of the systems while providing higher voltages and stored energy. The capacitor power versus voltage curves (figure 1.10) illustrate the cause of the significant effect of adding the piezoelectric. Recall that $V_{PV,\,max} = 6$ V. After this voltage, the solar cell is no longer able to contribute and all of the photogenerated current, I_L, dissipates over the pn-junction of the cell, D_{PV}. Figure 1.10(a) shows that just before the maximum solar voltage level, the multi-source topologies switch from closely following the charging curve of the solar harvester to following the charging curve of the piezoelectric harvester. This can be described as the charging curve being separated into a "solar-dominant" and a "piezo-dominant" region for SPS and SPP topologies. Note that the upper envelope is used to represent the power of the SPP and SPS topologies for $V_{CL} > 6$ V. The upper envelope is

used for the entire range of voltages for the P topology. Therefore, for the multi-source topologies, the high average power solar cell is only contributing power for a small fraction (1%) of the entire charging time. The rest of the charging is dominated by the low average power piezoelctric harvester. a

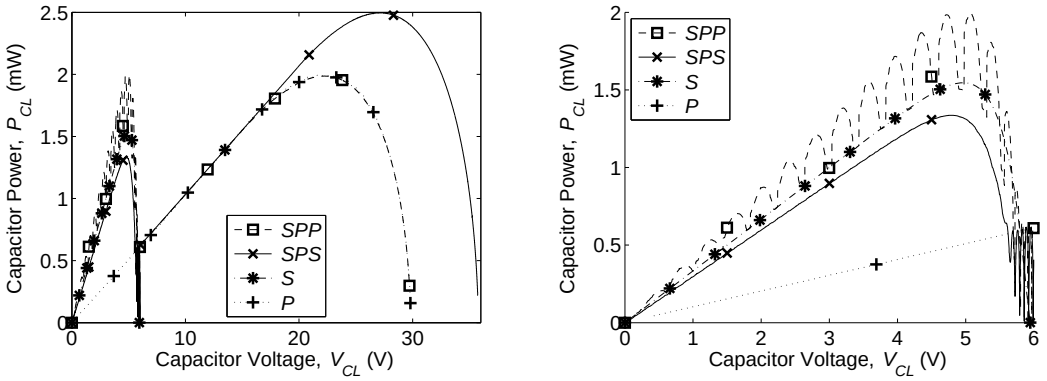

Figure 1.10: The capacitor power as a function of voltage for the SPS, SPP, P, and S topologies

Figure 1.10 also illustrates a significant difference between the SPS and SPP topology power behavior while $V_{CL} < 6$ V. The SPP topology curve shows visible oscillations at the rectified piezoelectric frequency constructively added onto the S topology curve. Therefore, during the "solar-dominant" section of the charging curve for the SPP topology, both the solar cell and the piezoelectric are contributing comparable amounts of power, resulting in a power increase over just the S topology itself. The same behavior is not seen during the "solar-dominant" section of the SPS charging curve.

The advantages of the SPP topology can be seen by examining the results of the schemes when only the period where the photovoltaic can contribute is considered (table 1.2). These results would occur if the storage capacitor is discharged by the load such that $V_{CL} < 6$ V always. As the table shows, in this

situation the average power, maximum power, and charge time results are better for the SPP topology than the S topology.

Table 1.2: Charging statistics for energy harvesting circuits for $V_{CL} < 6$ V

	S	P	SPS	SPP
Final voltage, V_f (V)	5.9	5.9	5.9	5.9
Final stored energy, E_f (mJ)	1.7	1.7	1.7	1.7
Charge time, t_f (sec)	1.9	10	2.4	1.8
Average power, P_{avg} (mW)	0.89	0.17	0.72	0.96
Maximum power, P_{max} (mW)	1.5	0.61	1.3	2.0

From these results, it can be said that the choice between the multi-source topologies depends on the characteristics of the load. For a high-power, low-duty cycle load, the SPS topology would prove effective due to its ability to store significant amounts of energy at once. An example would be wireless sensor node communication. The data transmission power requirements for the integrated RF transmitter in the MSP-CC430 microcontroller are 37.5 mW for receiving and 24-43.5 mW for transmitting. For energy harvesting solutions with maximum power levels not in this range, energy storage solutions are necessary. The high energy storage capabilities of the SPS topology will allow the system to better provide the short bursts of power necessary. For a low-power, low-duty cycle load, the SPP topology would prove effective due to its higher instantaneous power characteristics when $V_{CL} <$ 6 V. This will allow for the energy harvesting system to directly power the load, store energy, and significantly reduce the overall system mass by decreasing the size of the battery.

Solar and piezo - $r \ncong 1$

For multi-source energy harvesting systems, the power outputs of the two systems will not always be approximately equal to one another. As the solar cell will be subject to diurnal cycles as well as weather patterns, the output will vary significantly over the course of just a day. Figure 1.11 shows the maximum power of the multi-source topologies for the storage capacitor as the power ratio, r, given by equation (1.7), varies. Specifically, the piezoelectric parameters stay constant to produce the 2 mW maximum power output and the solar parameters vary. As r increases beyond one, the maximum power for the SPP topology is consistently greater than that of the SPS topology. This is a result of the additional piezoelectric power added on top of the SPP topology during the "solar-dominant" section of the charging curve. This plot also shows that for $r > 1.75$, the maximum power of both systems increases linearly with the solar cell. This means that there are no negative effects of having the solar cell at a significantly higher power output level that are not present for the case of $r \approxeq 1$.

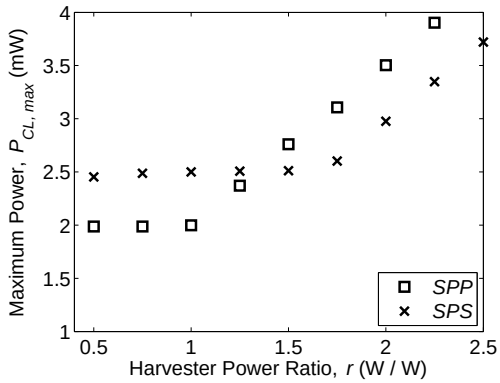

Figure 1.11: The maximum capacitor power as r varies for the SPP and SPS topologies

Two other cases of interest are when one of the harvesters is not producing any power output. These instances can be equated to nighttime for the solar cell and periods of calm winds or no vibrations for the piezoelectric. As figure 1.12(a) shows, when the solar cell is not producing any power, the charging curves for both of the multi-source topologies closely match that of the P topology. Figure 1.12(b) shows the same is true when the piezoelectric is not producing any power. These results show that the circuit architectures for the SPS and SPP successfully isolate the harvesters from one another, preventing power from dissipating over one or the other. This characteristic is key for a multi-source topology as part of the advantage of this type of system stems from the ability of the two energy sources to compliment one another.

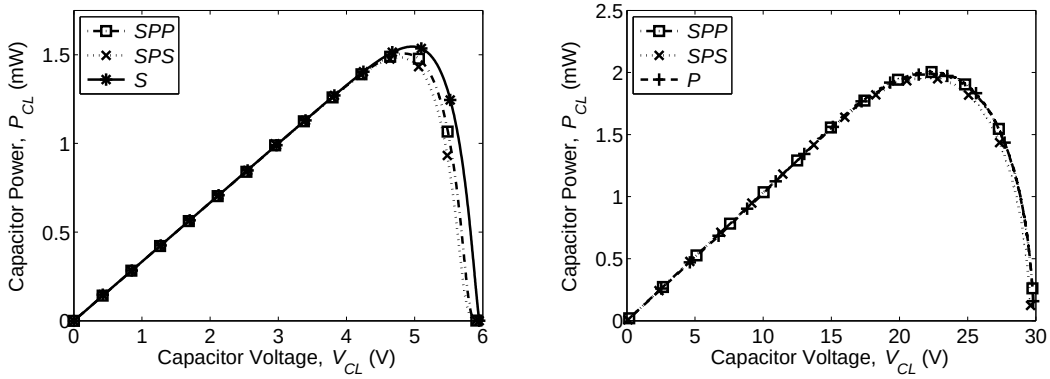

Figure 1.12: The capacitor power as a function of voltage for the SPS, SPP, P, and S topologies when the solar cell (a) and the piezoelectric (b) are not producing any power

1.2.4 Multi-source: array of piezos

In the case of an array of piezoelectrics, both harvesters use the same method of transduction. However, differences between the signals can arise due to small

differences between the harvesters. As illustrated by the set of equations representing the AC signals of the two harvesters (equation (1.9)), a phase angle, ϕ, a difference in frequency, Δf, and a difference in amplitude, ΔA, can occur. The nature of the differences depends highly on the method of excitation. For fluid flow excitation, frequency and phase differences would be expected more often than for mechanical vibrations. However, for all cases, amplitude differences would be a major concern due to the difficulty in manufacturing multiple piezoelectric harvesters with the same natural frequency.

$$\begin{aligned} V_{P1} &= A_{P1} \sin\left(f_{P1} * t\right) \\ V_{P2} &= A_{P2} \sin\left(f_{P2} * t + \phi\right) \end{aligned} \tag{1.9}$$

A standard piezoelectric harvesting system served as the control for comparison (figure 1.4) to evaluate the performance of the multi-source circuit topologies. This control harvester was always at the baseline presented in section 1.2.1. All of the component characteristics for the multi-source topologies are detailed in that section as well. Throughout the analysis, a subscript PPS denotes the series and a PPP the parallel multi-source harvesting topologies.

Array of piezoelectrics - series PPS topology

The two piezoelectric energy harvesters are placed in series after rectification for the passive series circuit topology (figure 1.13). The potential advantages of this topology are the same as in the SPS topology, namely higher storage capacitor voltages and energy levels through the summation of A_{P1} & A_{P2}.

In the absence of differences between the two signals, the charge time and the final voltage are both twice that of the P topology. However, since the final

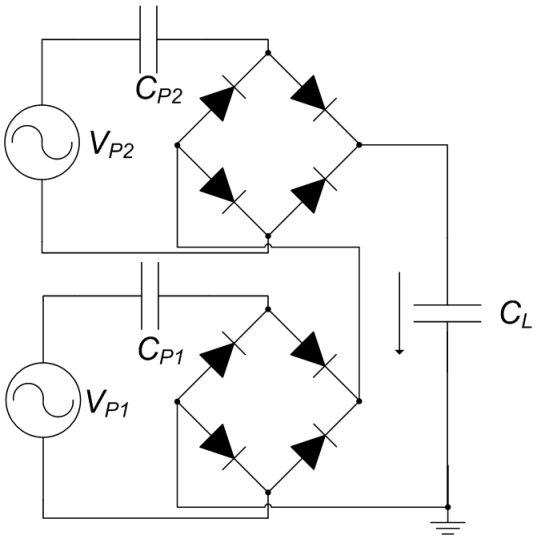

Figure 1.13: Series passive circuit topology, PPS

stored energy is four times that of the P topology, the average power doubles. The maximum power is double that of the P topology as well. Therefore, in the absence of differences between the two signals, the PPS topology constructively combines the power from the two systems very effectively.

Array of piezoelectrics - parallel PPP topology

In the parallel topology, the piezoelectric harvesters are placed in parallel after rectification (figure 1.14). This topology has the same potential advantages as the SPP topology, namely constructive current interference.

In the absence of differences between the two signals, the final voltage and stored energy level is equal to that of the P topology. However, the charge time is half that of the P topology, resulting in double the average power. The maximum power is double that of the P topology as well. As with the PPS topology, in the absence of differences between the two signals, the PPP topology con-

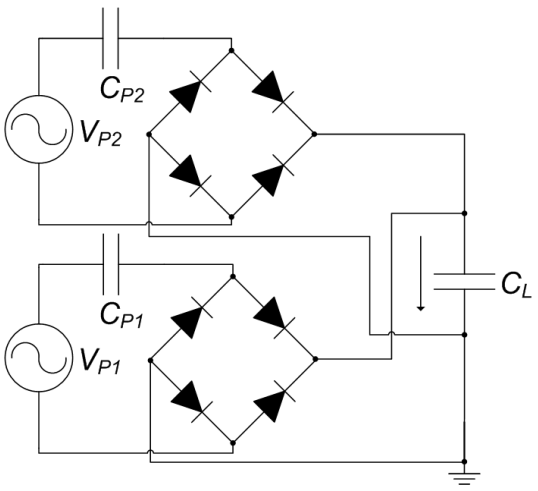

Figure 1.14: Parallel passive circuit topology, PPP

structively combines the power from the two systems very effectively.

Array of piezoelectrics - phase angle, ϕ

When a phase angle is introduced between the two harvesters in the multi-source topologies, the results of the simulations show that the storage capacitor charging is significantly affected. Figure 1.15 shows the effects of a varying phase angle on the capacitor final stored energy and average power. For the PPS topology, the capacitor final voltage level, final stored energy, and average power all decrease as the phase angle increases. The PPP topology remains unaffected. This can be explained by considering that for the individual piezoelectric harvesters to send current to the storage capacitor in the PPS topology, its rectified voltage must be higher than the sum of the storage capacitor voltage and the rectified voltage from the other piezoelectric harvester. When the two harvesters are out of phase, the rectified voltage from one of the piezoelectrics reaches its peaks before the other, creating periods of time where one of the har-

vester's voltage level is too low to conduct current. This does not occur in the PPP topology because the two piezoelectrics and the storage capacitor must all be at the same voltage level at all times.

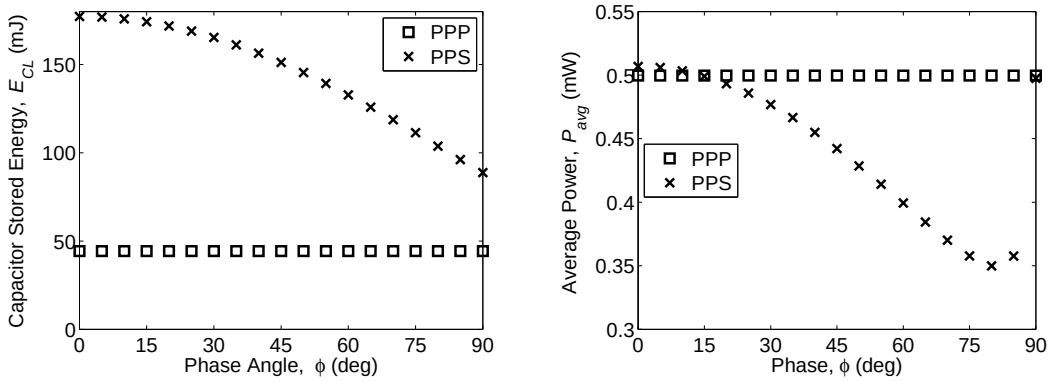

(a) (b)

Figure 1.15: The capacitor stored energy (a) and the average power (b) for the PPP and PPS topologies

Figure 1.16 shows how the instantaneous storage capacitor power is affected for both of the topologies. For the PPS topology, the maximum power level decreases along a quartic curve with respect to the capacitor voltage level (figure 1.16(a)). For the PPP topology, it decreases linearly until about 80°, at which point it starts increasing again (figure 1.16(b)). This means that as the phase between the two signals varies, the capacitor voltage at which the harvester system's peak performance occurs varies. It has been reported that a piezoelectric harvester charging a capacitor through a full-bridge rectifier experiences its maximum power levels, or peak performance, at half of the final charged voltage of the capacitor [76]. Since the final charged voltage of the capacitor is changing in the PPS topology, the capacitor voltage associated with the peak performance changes as well. For the PPP topology, the variation in the peak performance capacitor voltage is caused by the variations in destructive and

constructive interference between the harvester rectified voltages mentioned earlier.

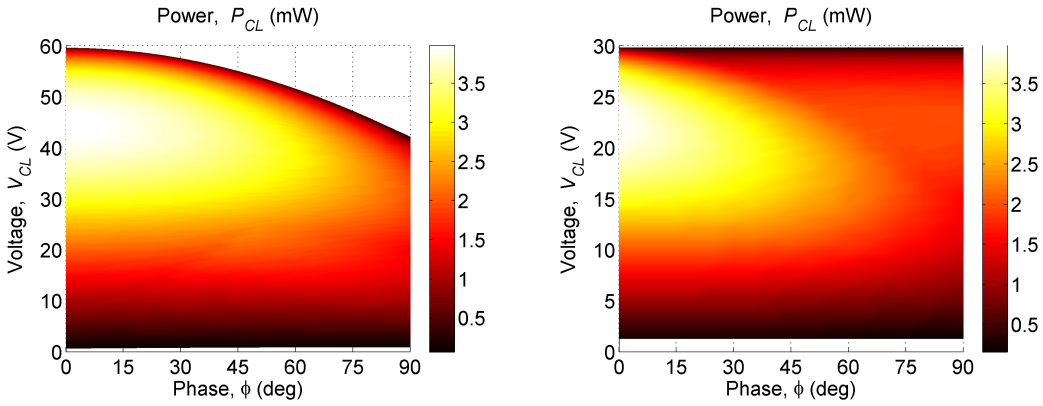

Figure 1.16: Upper envelope of the instantaneous power for the PPS (a) and PPP (b) topologies as ϕ varies

The performance of the passive multi-source topologies is significantly affected by a phase angle between the two harvester signals. The PPP topology performs more reliably than the PPS topology as only the maximum power level is affected with a phase angle. For the PPS topology, the final stored energy and average power levels are affected as well. The choice between the two topologies depends on the nature of the excitation signals. With machine vibrations, the response will be relatively predictable and the choice much simpler. However, with a stochastic excitation such as wind energy, knowing whether the phase angle between the two signal varies with any consistency or is stochastic itself will dictate which topology will perform better in this regard.

Array of piezoelectrics - frequency difference, Δf

A frequency difference, Δf, between the two harvesters causes the phase angle between the two signals to vary at a rate directly related to the frequency difference. This interaction creates a ripple in the charging curve for the PPS topology (figure 1.17). As the frequency difference between the two harvesters increases, the charging curve converges to a lower level. However, for the PPP topology, the charging curve remains constant for $\Delta f \neq 0$.

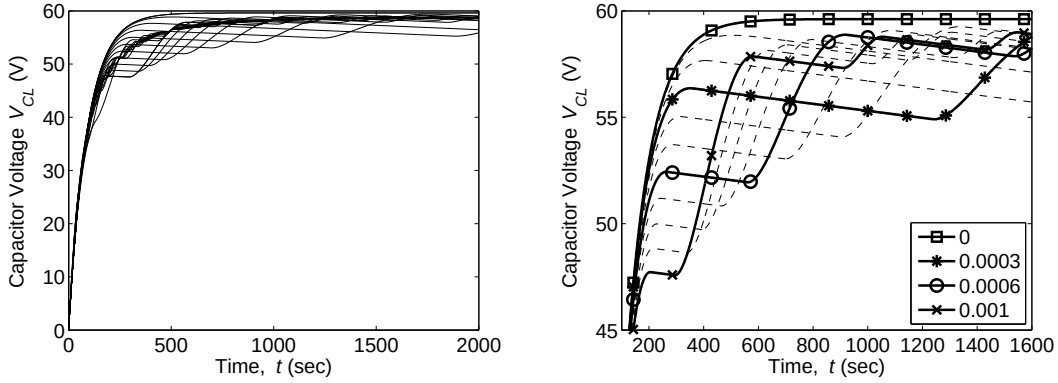

Figure 1.17: Capacitor charging curves as a function of Δf for the PPS topology

The reason for the ripple in only the PPS topology can be explained by looking at the voltage and power curves of the storage capacitor simultaneously with respect to time (figure 1.18). For a $\Delta f = 0$ Hz (a), both the capacitor voltage and power are smooth, however when a $\Delta f = 0.001$ Hz (b) is introduced, significant changes occur in the power curve. The power curve changes from the normal smooth curve for piezoelectric energy harvesting to a series of pulses; power is no longer flowing in a consistent manner, causing the capacitor to charge in bursts. As mentioned in the previous section, when the signals are out of phase they reach their peak voltages at different times and sum to a

lower amplitude than if the phase angle was zero. With a frequency difference, the phase angle is constantly varying and most of the time the signals are not summing to their maximum amplitude. This causes significant periods where the harvester voltages are too low to charge the capacitor and results in the pulses of power shown in figure 1.18(b).

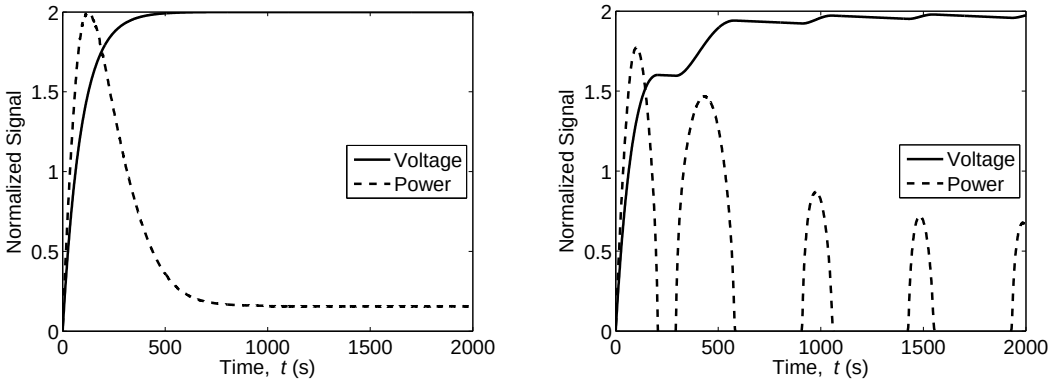

Figure 1.18: Normalized storage capacitor voltage and instantaneous power for Δf = 0 Hz (a) and 0.001 Hz (b) for the PPS topology

The effect that a frequency difference has on the upper envelope of the instantaneous power curves is shown in figure 1.19. While the voltage curve for the PPP topology is not adversely affected by the Δf, the power is. It creates significant oscillations between constructive and destructive interference, causing these erratic ripple patterns for both the PPP (b) and PPS (a) topologies. This behavior would complicate power management systems controlling the capacitor charging to maintain operations in the maximum power range, as the system could easily slip from a high power region to a low power region even if limited to a small capacitor voltage range. However, if any frequency difference is expected between the two harvesters, the PPP topology is less affected.

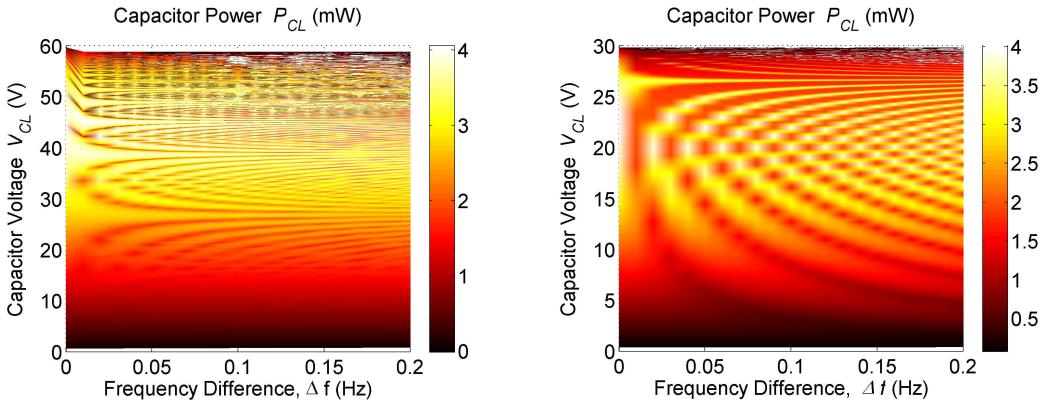

(a) (b)

Figure 1.19: Upper envelope of the instantaneous power for the PPS (a) and PPP (b) topologies as Δf varies

Array of piezoelectrics - amplitude difference, ΔA

Another possible difference between the two harvesters is the amplitude of the piezoelectric voltage, ΔA. When varying ΔA, the first expected result is that the final stored energy for the PPS topology decreases linearly with an increasing ΔA (figure 1.20). As the voltage signal from one of the harvesters decreases in amplitude the sum of the amplitudes decreases, causing a decrease in the final charged voltage of the capacitor. Also, the final stored energy for the PPP topology should not change as the voltages of the two harvesters are not summed. However, it was mentioned earlier that the voltages of the rectified outputs from the two harvesters and the storage capacitor must be equal at all times as they are all in parallel. In this instance, when the voltage of one harvester exceeds that of the other, the lower voltage harvester stops contributing power when $V_{CL} > A_P$ and the difference between the two is taken up as blocking voltages by the full-bridge rectifier. The full-bridge rectifiers successfully isolate the harvesters from one another in the PPP topology and allow the storage capacitor to charge to the voltage of the higher piezoelectric harvester.

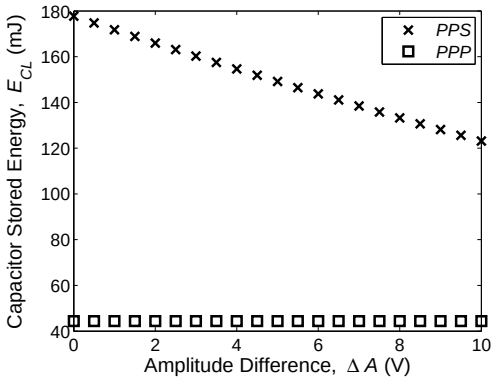

Figure 1.20: Final capacitor stored energy as a function of ΔA

The lower voltage harvester no longer contributing when $V_{CL} > A_P$ significantly affects the average power of the PPP topology. Figure 1.21 shows the average power for both topologies as ΔA increases. While the PPS topology shows a linear decrease in the average power corresponding with the decrease in the final capacitor voltage, the PPP topology exhibits an exponentially decaying average power down to an asymptote. This can be understood as the amount of power contributed by the lower power harvester becomes negligible as the ΔA increases, and the average power converges to the average power of a single harvester, 0.25 mW. The fact that this is an exponential decrease and not a linear one shows that even small ΔA values have significant affects on the performance of the PPP topology.

These trends are exhibited as well in the upper envelopes of the instantaneous power for the storage capacitors (figure 1.22). For the PPS topology, the maximum capacitor voltage decreases linearly, and the capacitor voltage at the maximum power decreases linearly at the same rate. For the PPP topology, there is a clear drop-off in the power levels following along a line starting from $V_{CL} = 30$ V at $\Delta A = 0$ V and intersecting with $V_{CL} = 0$ V at $\Delta A = 30$ V. This

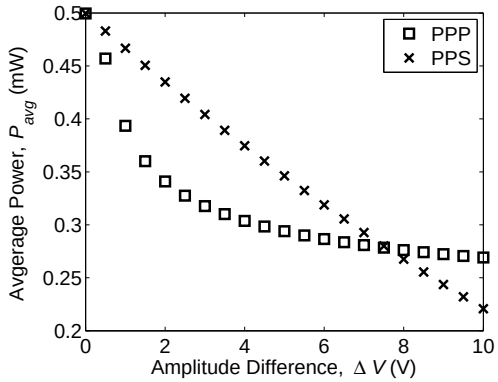

Figure 1.21: Topology average power as a function of ΔA

line represents the point in the charging curve at which the lower voltage harvester ceases to contribute power to the capacitor charging. As a result, the PPS topology is insensitive to performance degradations from a ΔA not caused by the different overall voltage levels. However, the PPP topology is affected by voltage incompatibilities between the lower voltage harvester and the storage capacitor, significantly affecting the topology's average power and maximum power levels.

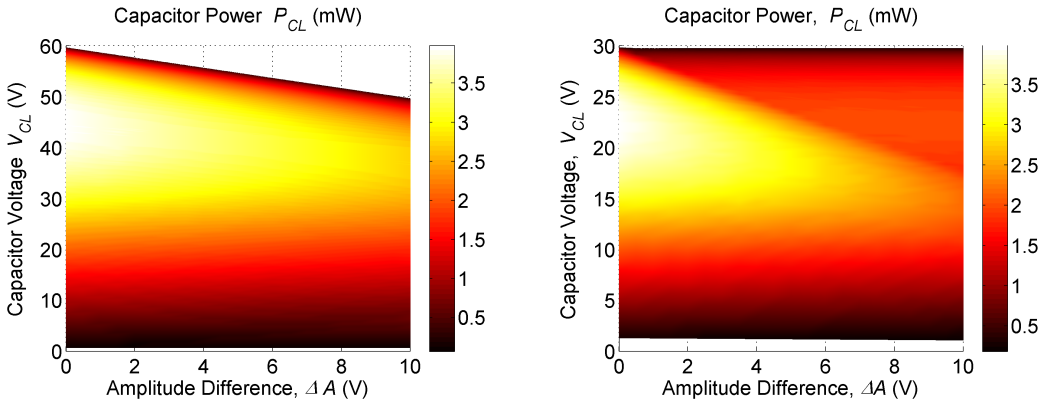

(a) (b)

Figure 1.22: Upper envelope of the instantaneous power for the PPS (a) and PPP (b) topologies as ΔA varies

1.3 Conclusions

Two, passive multi-source energy harvesting systems were explored as possible methods to vastly increase the robustness and effectiveness over single harvester systems. The piezoelectric circuit model used is an ideal model applicable to piezoelectric harvesters with low electromechanical coupling. Further examinations of specific instances of these schemes will utilize a more complex piezoelectric circuit model, such as the one presented by Elvin and Elvin [22]. This will allow for the isolation of the effects of the ideal signal interaction observed here and the electromechanical coupling, providing a thorough understanding of the schemes.

The first was the combination of a piezoelectric and a photovoltaic into both a parallel (SPP) and a series (SPS) topology. When the capacitor was allowed to fully charge, the SPS topology exhibited higher final stored energy levels than would normally be available with either the piezoelectric harvester (P) or the solar harvester (S). The higher stored energy levels lends the SPS topology toward high load, low duty cycle applications where the bursts of power needed are significantly above that either the solar or the piezoelectric are capable of providing. Both the SPS and SPP topologies exhibited "piezo-dominant" and "solar-dominant" charging periods, as the solar harvester provided high power levels below its maximum voltage and the piezoelectric charged the storage capacitor up to its higher voltage level. The SPP topology showed increases in the maximum power during the "solar-dominant" period as the power from the two harvesters summed. Therefore, the SPP topology lends itself toward low load, high duty cycle applications as the storage capacitor voltage can be discharged below the solar maximum voltage level to maintain the topology

harvesting in the high power region. When the power output from the two harvesters are not equal, the advantages exhibited by each respective topology were not significantly affected. Also, the circuit architecture was shown to effectively isolate the two harvesters from one another such that when one harvester is not producing any power, the other harvester charging the capacitor unimpeded.

For small, low-power piezoelectric energy harvesters, array configurations present a significant design tool for developing energy harvesting systems. An array of piezoelectrics, multi-source harvesting scheme was explored in both a series (PPS) and a parallel (PPP) topology. Both the series and the parallel topology doubled the instantaneous maximum power available from a single harvester. Also, the series topology provided the advantage of a higher available voltage level and final stored energy levels. However, the introduction of differences between the two harvesters significantly degraded the performance of these topologies. The series topology proved to be highly sensitive to phase angles and frequency differences between the harvesters. On the other hand, the parallel topology was significantly affected by an amplitude difference. Also, the maximum instantaneous power levels were affected by phase angles and frequency differences for the parallel topology, while the average capacitor charging rate was unaffected. Both systems also exhibited beat phenomenons in their instantaneous power curves with respect to the voltage levels of the capacitors in the presence of a frequency difference. However, given an array of piezoelectric harvesters where few differences are expected these passive, multiplicity of piezoelectrics multi-source topologies effectively harvest the available energy while minimizing the necessary control and the number of components.

Future considerations of these schemes for specific instances will examine the use of the power optimization methods mentioned in the Introduction. Specifically, the question of whether a single power optimization technique could be applied to the passive multi-source schemes presented here as opposed to separate techniques for each harvester will be addressed. This will allow for harvesting significantly more power while only suffering from the overhead of a single power optimization technique.

CHAPTER 2

A LOW-LOSS HYBRID RECTIFICATION TECHNIQUE FOR PIEZOELECTRIC ENERGY HARVESTING [2]

2.1 Introduction

The continual advances in small-scale electronics has increased the demand for the development and use of embedded systems, or remote battery-powered systems. However, the limited capacity of small-scale energy storage technology necessitates methods for generating *in situ* power. As a result, energy harvesting has gained significant attention in recent years with the goal of creating self-reliant embedded systems.

Ambient vibration sources exist in many locations and are of particular interest as a potential power source when solar power is not readily available. Over the past couple of decades, a significant body of work explored the use of piezoelectric vibration energy harvesting devices to power embedded systems [65, 2]. The majority of piezoelectric energy harvesters reported in the literature produce relatively small amounts of power, in the mW-μW range. Efficient power conditioning is key for piezoelectric vibration energy harvesting to produce the power levels necessary for embedded systems.

One challenge present for all piezoelectric energy harvesting systems is that the transducer power output is inherently AC while the majority of embedded system electronics require a constant DC source. A full-bridge rectifier using semiconductor diodes is the most common configuration (figure 2.1). Table 2.1

[2] This chapter was originally published as a journal article in *Smart Materials and Stuctures* [55] and is reproduced here with permission of IOPscience.

illustrates the difficulty of designing a high-efficiency, low-power rectifier using semiconductor diodes. For diodes with low forward voltage drops, V_F, the reverse leakage current, I_R, is typically quite high. While lower forward voltage drops allow for higher output voltages and the ability to rectify lower voltage signals, the higher reverse leakage current leads to drops in efficiency as well [13, 14]. Lastly, the maximum DC blocking voltage, $V_{R,max}$, must also be greater than the maximum piezoelectric voltage amplitude to prevent diode failures.

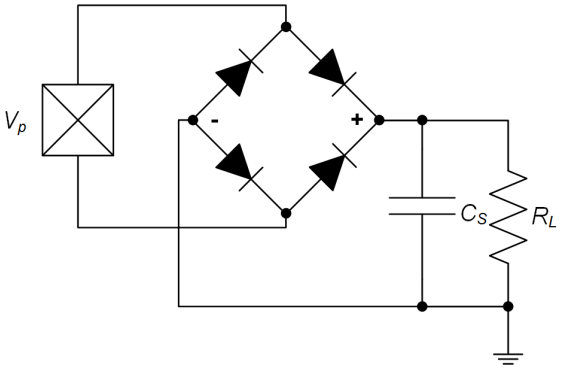

Figure 2.1: Schematic of a standard piezoelectric charging circuit using a semiconductor diode full-bridge rectifier.

Table 2.1: Characteristics of common commercially available semiconductor diodes.

Manf. Num.	$\boldsymbol{V_F(V)}$ **@** $\boldsymbol{I_F(A)}$	$\boldsymbol{V_{R,max}(V)}$	$\boldsymbol{I_R(\mu A)}$ **@** $\boldsymbol{V_R(V)}$
1N5818	0.70 @ 1.0	30	1000 @ 30
90SQ030	0.375 @ 1.0	30	1750 @ 30
SB330	0.35 @ 1.0	30	500 @ 30
1N4148	1.0 @ 0.1	100	0.025 @ 20
1N914	0.9 @ 0.1	75	0.025 @ 20

Multiple techniques for high-efficiency AC-DC rectification have been examined in the literature, most focusing on low-voltage piezoelectric energy harvesters. Synchronous rectification uses active switching instead of passive semiconductor diodes. This is typically performed using the comparator-controlled

MOSFET semiconductor switches shown in figure 2.2 [35, 25, 54, 53]. These methods report significantly lower forward voltage drops and the ability to rectify very-low-voltage signals. Voltage doubler and multiplier configurations are also of interest due to their ability to raise low-voltage input signals to the levels needed for batteries and embedded systems electronics [13, 14, 16, 42]. Novel configurations have been examined as well, such as alternating between a non-inverting and an inverting boost converter in parallel [44, 21]. However, all of these methods require the use of active components with external power sources at voltage levels greater than the input voltage level. This adds the complexity of a startup mechanism to raise the available voltage before achieving these efficiency levels. As a result, there is still a significant need for a simple, high-efficiency AC-DC rectification method.

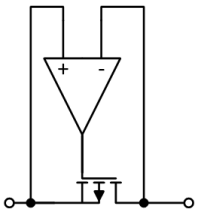

Figure 2.2: Schematic of an active switch using a comparator and a MOSFET

This work examines a low-loss mechanical AC-DC rectification scheme for piezoelectric energy harvesting using magnetically actuated reed switches. The concept was first introduced in [69], where the idea is presented and initial experimental data of the system operation is shown. The reported results suffer from the effects of gravity due to the vertical excitation of the harvester. This work takes the next step, showing the results of a horizontally-aligned experimental setup, removing the effect of gravity from the experiment. It also develops a theoretical model to describe the expected performance over a range of conditions. It is organized as follows: first, the mechanical rectification with

reed switches technique is described. A theoretical model of its performance is developed to explore the operating conditions where its use is desirable. A novel hybrid method is then introduced and examined to create a very appealing low-loss AC-DC rectification technique. The technique is then experimentally demonstrated and verified to produce higher output voltage levels than a semiconductor diode full-bridge rectifier.

2.2 Reed switches

A reed switch is comprised of two thin and flat cantilevered leads placed in very close proximity inside of a vacuum sealed casing (figure 2.3). When a magnetic field is introduced, either using a hard magnet or an inductive coil, the individual leads are magnetically polarized in the direction of the field. This causes the ends of the leads in the vacuum-sealed casing to be oppositely poled. When the strength of magnetic attraction overcomes the stiffness of the leads, they close and create a very low resistance electrical connection. The switch opens when the magnetic field is removed or becomes too weak.

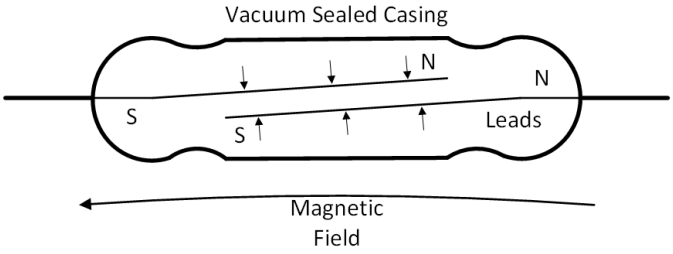

Figure 2.3: Diagram of a magnetically actuated reed switch

Figure 2.4 illustrates the expected behavior for the reed switches when actuated using a permanent magnet whose poles are aligned along the leads of

the switch. Figure 2.4(a) shows the behavior as the relative separation between the center of the magnet and the reed switch is varied parallel to the leads. Figure 2.4(b) shows the behavior for the relative motion perpendicular to the leads. There are three regions shown: 'open', 'hold', and 'close'. The 'close' and 'open' regions correspond to when the leads are in contact and not in contact, respectively. The 'hold' region represents the magnetic hysteresis exhibited by the switches. When the magnet is nearing the reed switch and crosses into the 'hold' region from the 'open' region, the leads stay separated. The magnet must cross into the 'close' region for the force of magnetic attraction to be greater than the stiffness of the leads. However, when the magnet moves out of the 'close' region and into the 'hold' region, the leads stay attached due to the residual magnetic polarity of the leads. The magnet must cross into the 'open' region for the force due to the stiffness of the leads to be greater than the magnetic attraction. It is in this manner that reed switches exhibit magnetic hysteresis.

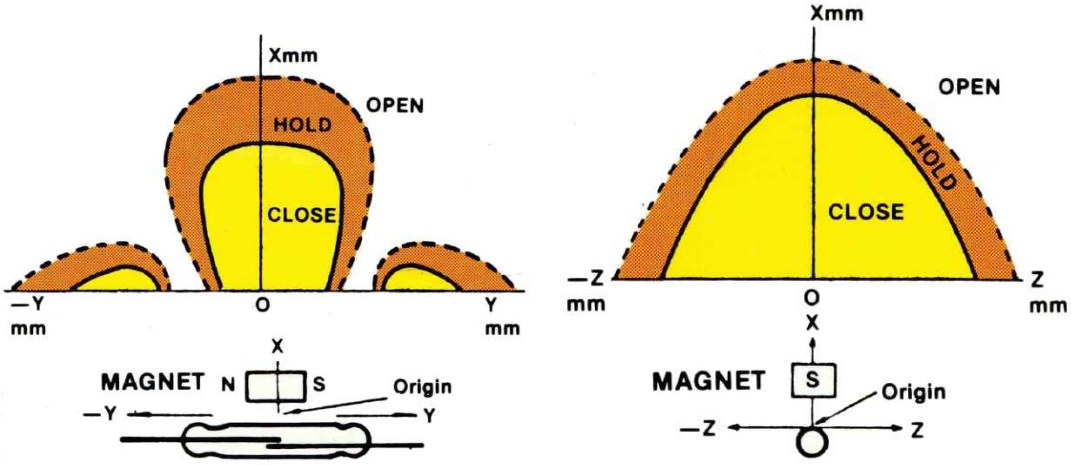

Figure 2.4: The 'close' and 'hold' regions which describe the behavior of a magnetically actuated reed switch [29]

Table 2.2 presents some pertinent specifications for a selection of commercially available small-scale reed switches. The contact resistance is denoted by

R_C, t_O is the operation time (including bouncing due to contact), t_R is the release time, l is the enclosure length, and d is the enclosure diameter. The contact resistances are minimal as expected. However, the mechanical nature of the switch results in significantly slower response times than those achievable with semiconductor switches. For instance, given a 0.75 ms operating time, if we assume a maximum acceptable lag time of a quarter-period, we would be limited to frequencies lower than approximately 333 Hz. It is significant to note, however, that the majority of environmental vibration sources explored for energy harvesting applications lie below this cutoff.

Table 2.2: Characteristics of small-scale commercially available reed switches.

Manf. Num.	$R_C(\Omega)$	$t_O(ms)$	$t_R(ms)$	$l(mm)$	$d(mm)$
MARR-5	0.1	0.75	0.3	19.69	2.66
MARR-1	0.1	0.75	0.3	19.05	2.66
KSK-1A35	0.15	0.5	0.1	10.5	1.95

2.3 Reed switch rectification

Mechanical AC-DC rectification by magnetically actuating reed switches utilizes the oscillatory motion exhibited by many vibration energy harvesters. Figure 2.5 shows an electromechanical schematic of the technique. As the cantilevered beam oscillates to its peak deflection, the magnetic tip mass causes the reed switches to close. To achieve the equivalent of full-bridge AC-DC rectification, two pairs of reed switches are used, SW_{P1} and SW_{P2}. The leads attached to the electrodes of the piezoelectric patch on the beam are split to one reed switch in each of the pairs. The outputs from the reed switches are then combined such that the reed switch in the first pair attached to the top electrode is connected to

the reed switch in the second pair attached to the bottom electrode. When the piezoelectric is producing a negative voltage, the pair of reed switches which are closed cause the output signal to be positive. When the piezoelectric voltage is positive, the output stays positive. It is by this arrangement of the switches that the signal is rectified.

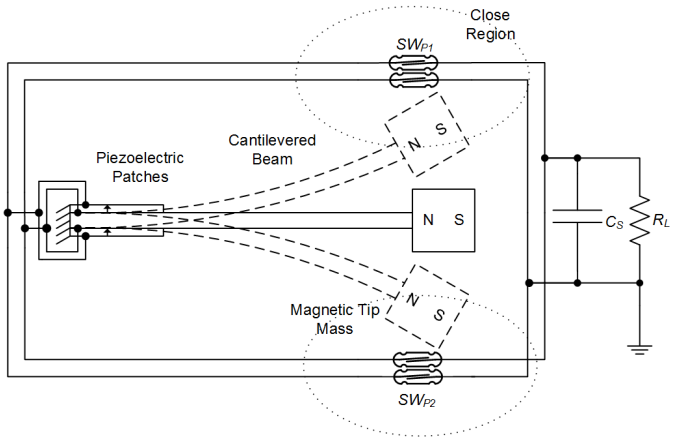

Figure 2.5: Electromechanical schematic of mechanical AC-DC rectification using magnetically actuated reed switches

The performance of the system is primarily dictated by the relationship between the tip deflection amplitude and the pull-in distance for the magnet and reed switch pair. It is also affected by the size of the "hold" region shown in figure 2.4, i.e., the amount of magnetic hysteresis exhibited by the magnet and reed switch pair.

2.3.1 Theoretical modeling

A numerical model of the voltage output for a half-period allows for the examination of the effectiveness of mechanical AC-DC rectification by magnetically activated reed switches. The model is evaluated over only an oscillation half-

period due to symmetry. Equation (2.1) shows the formulation of the models for the full-bridge rectifier using ideal diodes, V_{ideal}, an offset diode model, V_{offset}, and the mechanical reed switch rectification, V_{reed}. For the model, $V_\gamma = 0.4$ V.

$$V_{ideal} = Asin(2\pi t) \tag{2.1}$$

$$V_{offset} = \begin{cases} V_{ideal} - 2V_\gamma & : V_{offset} > 2V_\gamma \\ 0 & : V_{offset} < 2V_\gamma \end{cases} \tag{2.2}$$

$$V_{reed} = \begin{cases} 0 & : t < t_{delay} \\ V_{ideal} & : t_{delay} < t < t_{open} \\ 0 & : t > t_{open} \end{cases} \tag{2.3}$$

The proximity delay, t_{delay}, is the amount of time it takes for the magnet to enter the "close" region from the start of the half-period. The switch reopens at t_{open}, which is determined using equation (2.4). The magnetic hysteresis of the reed switch, n_{hyst}, is defined using the proximity delay. For instance, for a 50% hysteresis the switch stays closed for $t_{delay}/2$ seconds longer than it would with no hysteresis. For the purposes of this model, the "close" region is defined as the time $t_{delay} < t < T/2 + t_{delay} \cdot (n_{hyst} - 1)$. Figure 2.6 shows an example of the results of the numerical model as well as the effect of the magnetic hysteresis for a 10 V amplitude input signal. The line at 0.35 represents where the switch would close without hysteretic behavior and the line at 0.425 represents 50% hysteresis.

$$t_{open} = \frac{T}{2} - n_{hyst} \cdot t_{delay} \tag{2.4}$$

The analysis was performed for a range of input signal amplitudes, proxim-

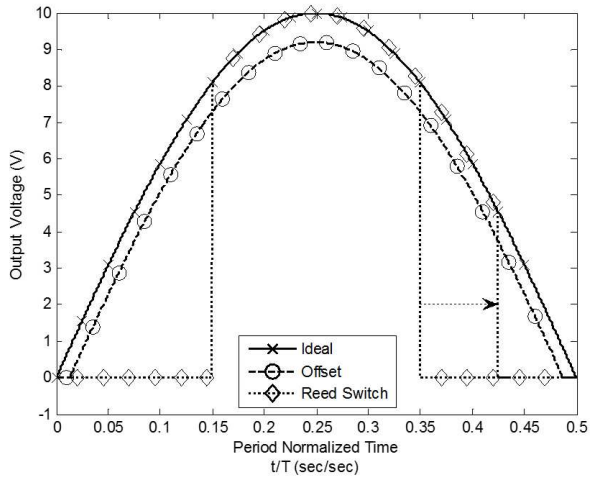

Figure 2.6: Example of the theoretical modeling results of an oscillation half-period. The arrow shows the effect of hysteresis on the switching behavior.

ity delay times, and hysteresis levels. Figure 2.7 presents the results of the cases with $n_{hyst} = 0\%$, 50%, and 100%. The RMS voltage values for the reed switch rectification method are represented by the plane. The results for the ideal and offset diode model rectifiers are shown by marked lines which outline the position of the planes. Note that the RMS voltage values for the diode rectification methods are independent of the proximity delay. When the plane is flat at zero volts, the reed switches never close during the oscillation half period and no current is conducted. As expected, this portion of the plane occurs where the proximity delay is greatest and its size varies with the amount of hysteresis.

The portions of the plane where the RMS voltage output is greater than the offset diode model represents the potential for higher power output and therefore greater conversion efficiency. It is in these instances where the proposed reed switch rectification method is preferable. Comparing figures 2.7(a), 2.7(b), and 2.7(c) illustrates that greater hysteresis values result in a larger set of conditions under which the reed switch method has higher RMS voltage output. This

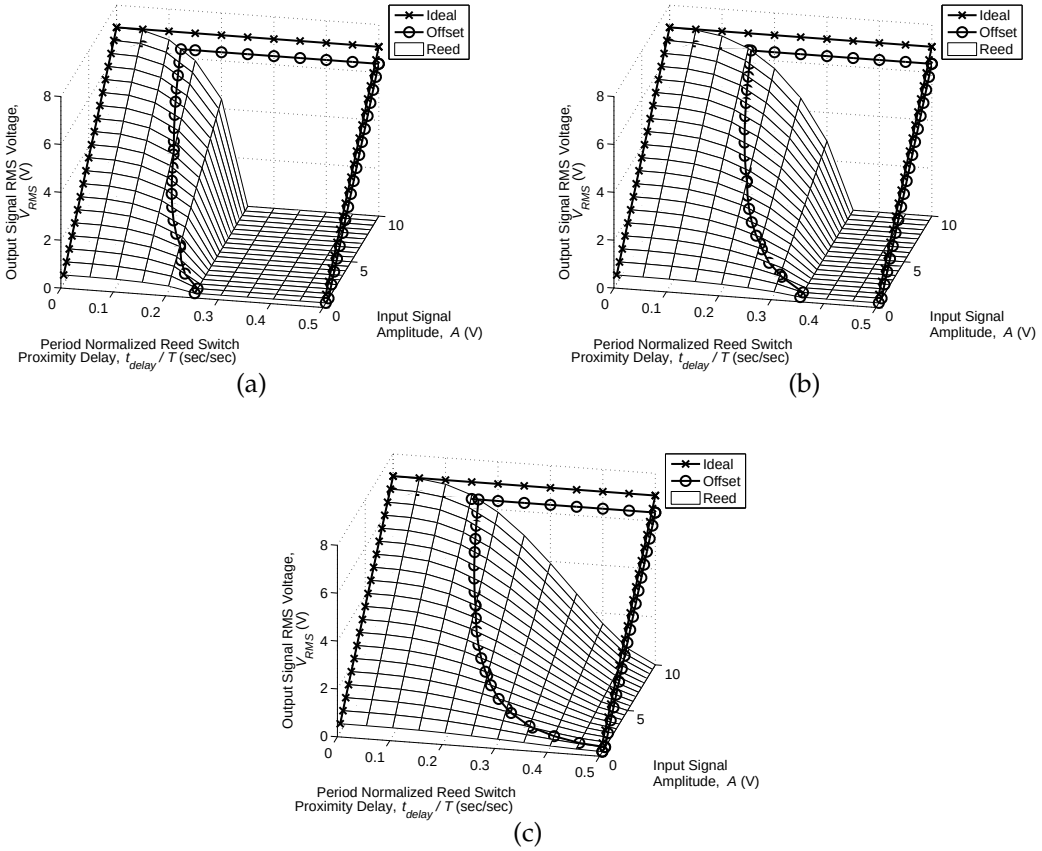

Figure 2.7: Results of the model showing the RMS voltage of the output signal as the reed switch proximity delay and the input signal amplitude vary for n_{hyst} = (a) 0%, (b) 50%, and (c) 100%.

is because with larger hysteresis levels the switch is closed for longer periods of time and a larger percentage of the signal is transmitted.

2.4 Hybrid rectification

The semiconductor diode and reed switch rectification methods both possess weaknesses which limit their application. For a diode rectifier, the threshold voltage and the forward voltage of the diodes limit the system performance by restricting it to higher voltage energy harvesting systems and decreasing the

conversion efficency. An advantage of the method is that as long as the threshold voltage is met, current can be conducted. For the reed switch rectification method, an advantage is that when the switches are closed there is no threshold voltage and the power dissipation is minimal. This allows for the use of the system with low-voltage energy harvesters and potentially increases the rectification efficiency. However, as shown in section 2.2, the switches are not always closed so current is not conducted 100% of the time. As a result, the reed switch rectification method cannot be expected to always be more efficient than a semiconductor diode rectifier.

The proposed hybrid rectification scheme takes advantage of the strengths of both the standard semiconductor diode and magnetically-actuated reed switch rectification methods simultaneously. Figure 2.8 shows the electrical schematic for the proposed hybrid rectification scheme. Placing a diode full-bridge rectifier in parallel with the reed switches allows for the transmission of electrical energy when the reed switches are open. When the reed switches are closed, the energy follows the path of least resistance through the low-loss reed switch from the high V_P to the lower V_{RL}. Note in the schematic that the reed switches are paired electrically as opposed to physically such as in figure 2.5.

2.4.1 Theoretical modeling

The theoretical model was extended to examine the hybrid rectification technique, as defined by equation (2.5). Again, only an oscillation half-period is analyzed. Figure 2.9 shows an example of the results with $n_{hyst} = 50\%$ and an input signal amplitude of 10 V.

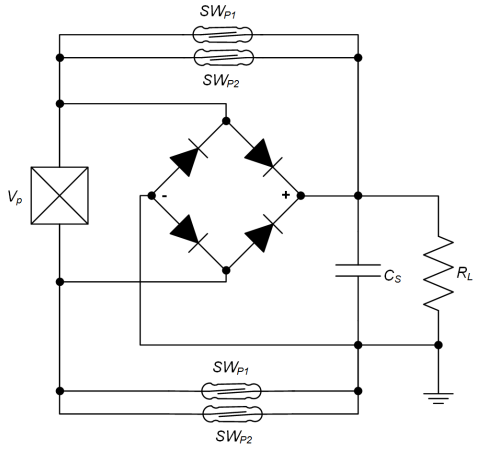

Figure 2.8: Electrical schematic of the proposed hybrid AC-DC rectification method using magnetically actuated reed switches and semiconductor diodes.

$$V_{hybrid} = \begin{cases} V_{offset} & : t < t_{delay} \\ V_{ideal} & : t_{delay} < t < t_{open} \\ V_{offset} & : t > t_{open} \end{cases} \tag{2.5}$$

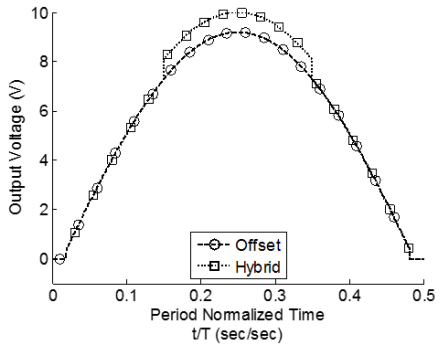

Figure 2.9: Example results of the numerical model of for the hybrid rectification scheme for n_{hyst} = 50%.

Figure 2.10 shows the results of the analysis for the hybrid rectification system for the cases where n_{hyst} = 0%, 50%, and 100%. The results of the hybrid model are represented by the plane. The results for the ideal and offset diode model are shown by marked lines which outline the position on the planes. For

the hybrid approach, the offset diode model plane now represents the baseline as opposed to zero for the reed switch results (figure 2.7). This result is important as it illustrates that according to this model the hybrid method always produces a higher output voltage than the offset diode method. As with the reed switch rectification method, the larger the hysteresis effects the higher the output RMS voltage. Note that the proximity delay point where the increase in performance starts for the hybrid rectification system is now independent of the input signal amplitude.

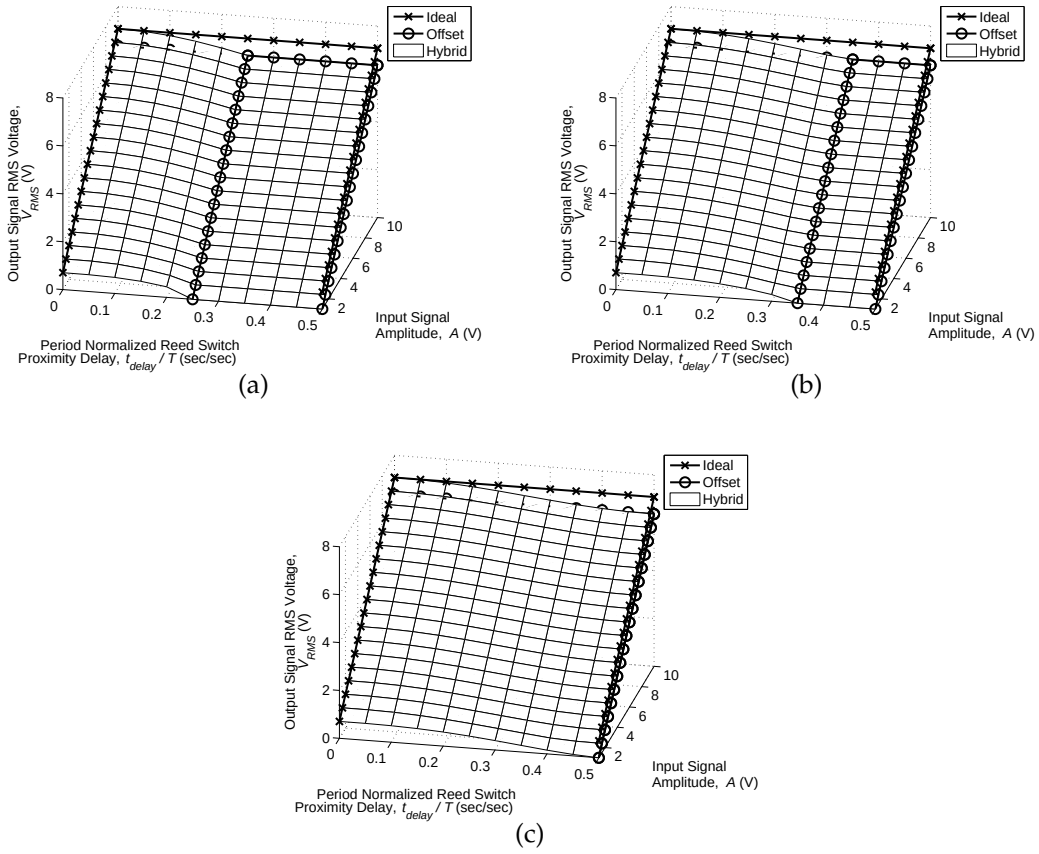

Figure 2.10: Results of the model for the hybrid technique showing the RMS voltage of the output signal as the reed switch proximity delay and the input signal amplitude vary for n_{hyst} = (a) 0%, (b) 50%, and (c) 100%.

2.5 Experimental validation

2.5.1 Experimental setup

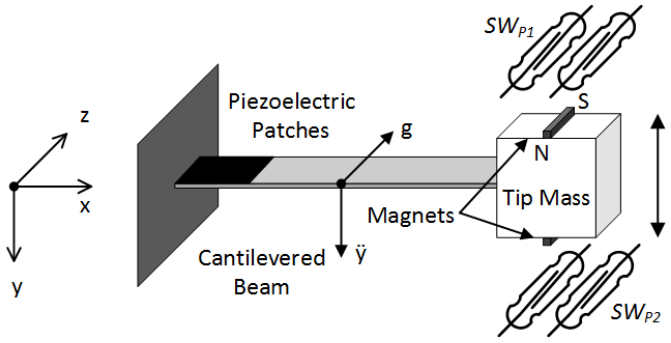

Figure 2.11: Mechanical schematic of the experimental setup for the AC-DC rectification by magnetically actuated reed switches methodology.

Figure 2.11 shows the schematic of the mechanical aspects of the experimental setup. Figure 2.12 shows a labeled picture of the actual setup. A 200.0 x 25.9 x 0.4 mm cantilevered beam served as the experimental prototype. As mentioned previously, the horizontal alignment of the beam minimized the effects of gravity on the experiment. A rapid-prototyped ABS plastic 32.5 g tip mass was secured 36.70 mm from the tip of the beam. This produces a first bending mode natural frequency of 5.07 Hz with a damping ratio of 0.00974. Two Midé QP16n QuickPack^{TM}piezoelectric patches with measured capacitances of 117 and 102 nF were epoxied to the base of the beam and connected electrically in parallel. Hamlin H-33 magnets attached to either side of the tip mass actuated the two Hamlin MARR-1 reed switch pairs. Reed switch holders, rapid-prototyped out of ABS plastic, were bolted to an aluminum x-channel frame to provide position control in all three axes.

The beam was attached to a Brüel & Kjæl 4809 electromagnetic shaker pow-

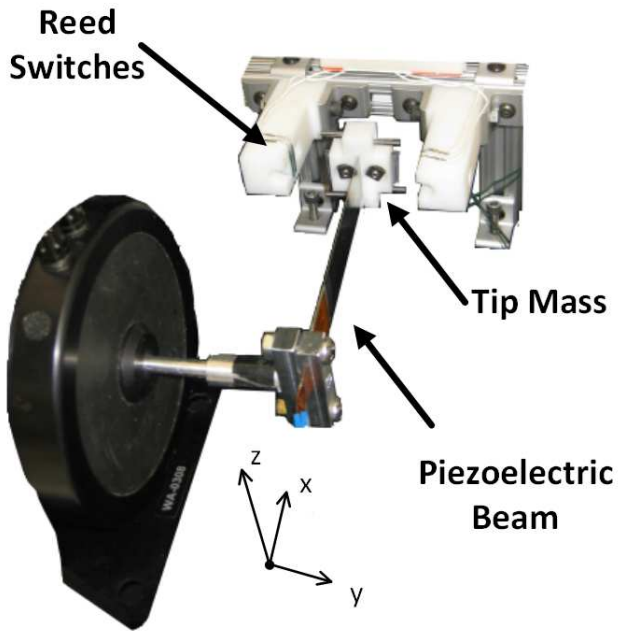

Figure 2.12: The experimental setup for mechanical AC-DC rectification by magnetically actuating reed switches.

ered by a Brüel & Kjæl 2718 power amplifier. The beam was excited off resonance at a constant 3.7 Hz to provide more predictability for the tip deflection amplitudes. The low damping ratio of the beam caused a very sharp peak in the response amplitudes at the first natural frequency. Slight variations in the setup would produce very significant changes in the tip deflection amplitude, the parameter of interest for the mechanical rectification method. Therefore, to set up the system for experimental validation of the proposed rectification method, greater control was chosen over increased power density levels.

The full bridge rectifying circuit used in conjunction with the mechanical rectifier consisted of four 1N5818 Schottky diodes, whose characteristics are listed in table 2.1. Figure 2.13 provides a closer view of the reed switches, the magnetic tip mass of the experimental setup, and the spacings used during the ex-

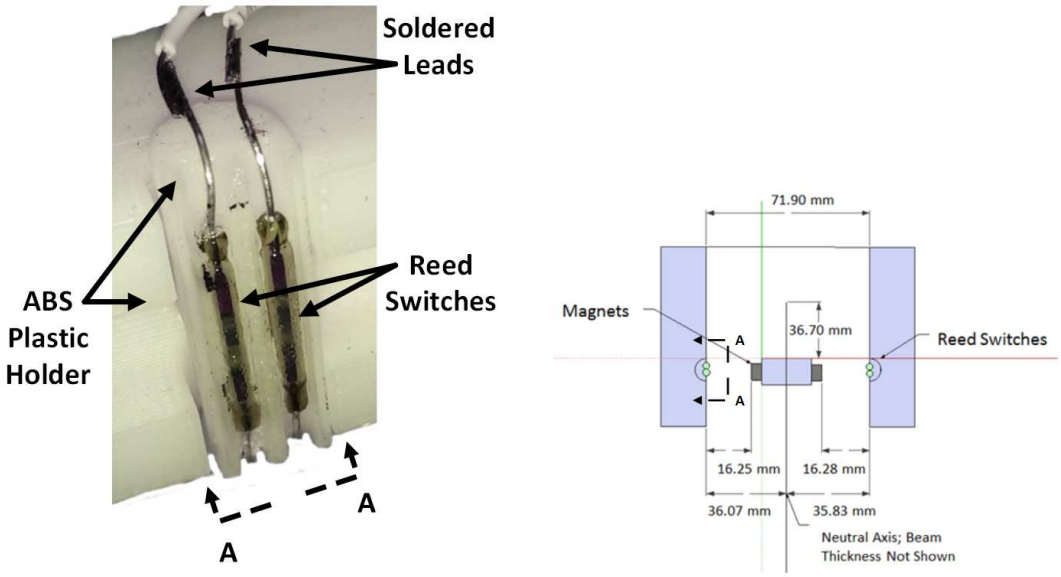

(a) (b)

Figure 2.13: (a) A close-up of the mounted reed switches and (b) the orientation of the reed switches with respect to the magnets on the tip mass.

perimental results reported herein.

2.5.2 Experimental results

The beam was excited at a tip deflection amplitude which actuated the reed switches. As the excitation frequencies were well below the operational limits of the reed switch, the tip deflection was the only concern for the experimental validation tests. It is important to note that the excitation frequency and amplitude were kept constant during all of the tests reported herein. The output voltage from the rectifiers was captured for a period of 3.75 oscillation cycles.

Figure 2.14 shows the experimental results of one and a half oscillation periods for all three tested setups: the semiconductor diode rectifier using 1N5818 Schottky diodes, the reed switch rectifier, and the hybrid methodology. Figure

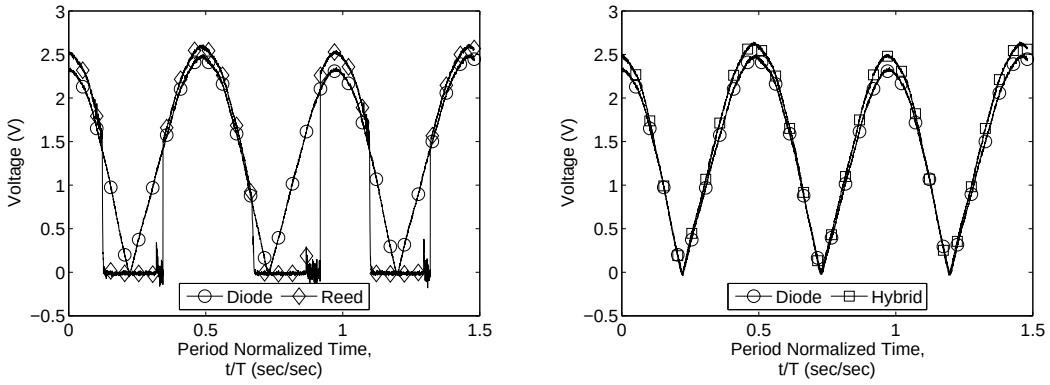

(a) (b)

Figure 2.14: The experimental results of (a) the reed switch rectification method and (b) the hybrid scheme compared to a semiconductor diode full-bridge rectifier.

2.14(a) shows the results of the reed switch experiment as compared to the diode rectifier. Note that when the switches are closed, the output voltage is always greater for reed switch rectification. The effect of hysteresis is also visible as the output voltage waveforms for the reed switch method are not symmetric about the peak. The hybrid rectification method shows that current is conducted when the reed switches are open (figure 2.14(b)).

Also of note for both experiments is the variation of the peak voltage from one half period to the next. Although not shown here, when viewed for the full 3.75 periods it is clear that the maximum voltage of the piezoelectric harvester is different when deflected in one direction compared to the other. This occurs consistently between all of the experiments no matter the electrical circuit attached to the harvester. Therefore, it can be attributed to the 15% asymmetry between the piezoelectric capacitances for the two patches.

Lastly, there is a noticeable difference in voltage between the standard diode waveform and the reed switch or hybrid rectification methods. This difference

is analogous to the semiconductor diode forward voltage and is a maximum of approximately 0.2 V (0.1 V for each diode). This is significantly smaller than the 0.7 V listed in table 2.1 for the 1N5818 at 1.0 A. The forward voltage is highly dependent on the load current level and the lower the current, the lower the forward voltage. Therefore a significantly smaller forward voltage is expected since the current levels are significantly lower than 1.0 A.

Table 2.3: The experimental RMS voltages calculated over 3.75 oscillation periods for the three rectification methods.

Rectification Method	$V_{RMS}(V)$
1N5818 Diode	1.62
Reed Switch	1.57
Hybrid	1.73

Table 2.3 displays the results of the three experiments. In this situation, the reed switch mechanical rectification method performs 3.1% worse than the Schottky diode rectifier. As the model shows, whether the reed switch method produces a higher RMS output voltage than the standard diode rectifier relies on the input voltage amplitude, the proximity delays and hysteresis levels. Figure 2.14(a) shows significant proximity delay for the second complete half period and this is the greatest contributor to the worse performance. This is corroborated by the performance of the hybrid system, which has a 6.8% higher RMS output voltage than the standard diode rectifier. By allowing the transfer of power when the reed switches are open the effect of the proximity delay is minimized and the performance increases. Note again that the exact positioning and tip deflection amplitude were the same between the reed switch and hybrid experiments.

2.5.3 Theoretical model validation

To verify the accuracy of the theoretical models for predicting the behavior of the rectification methods, the independent variables were matched to that seen in the experiment. Specifically, A = 2.64 V, t_{delay}/T = 0.114, $V_\gamma = 0.100$ V, and n_{hyst} = 0.500. The amplitude was chosen based on the maximum voltage seen from the three experimental results. Figure 2.15 shows the results of the model validation comparison. The offset diode model used for the semiconductor full-bridge rectifier shows the expected differences at the start and end of the half-period. The use of a piece-wise diode model, for example, would result in greater accuracy at these locations. However, it can be seen that the model not capturing this behavior does not significantly alter the results.

For the proposed rectification methods, the presented theoretical models show close agreement with the experimental results. The reed switch rectification model accurately captured the effects of the proximity delay and the hysteresis. The oscillations about zero before the switch fully closes are related to the bounce of the reed switch, which is when the two reeds strike one another and oscillate until reaching a closed steady state. This phenomenon was not captured by the model but has a limited effect on the overall results due to the low voltage levels. The not-quite instantaneous drop in voltage at the end of the conduction period (at $\approx$ 0.44 sec/sec) is also not captured. This phenomenon was seen in independent reed switch testing and is hypothesized to be the combined result of the non-zero release time and the non-zero contact capacitance.

The results of the hybrid rectification experiments show good agreement with the model in that has a higher RMS output voltage than both the diode and

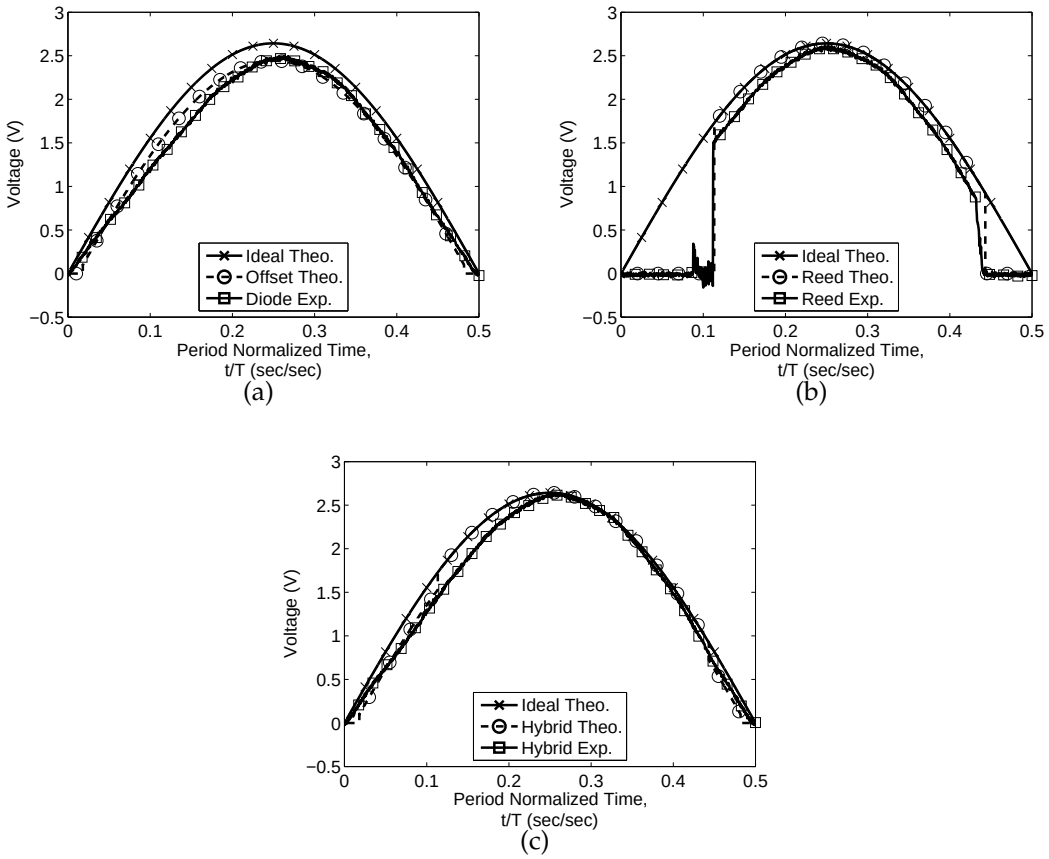

Figure 2.15: Comparison between the results of the theoretical model for A = 2.64 V, t_{delay}/T = 0.114, n_{hyst} = 0.500, and V_γ = 0.100 V for the (a) 1N5818 Schottky diode method, the (b) reed switch method, and the (c) hybrid method.

reed switch rectification methods. However, comparing waveforms shows that the model does not capture some of the experimental behavior. In the model waveform the voltage instantaneously jumps from the offset diode curve to the ideal diode curve when the reed switches close. In the experimental waveform this jump is not visible. This difference can be attributed to the assumptions made in the model: the use of the offset diode model, no reed switch contact resistance, as well as instantaneous close and release times for the reed switch.

Lastly, the overall voltage levels for the reed switch and hybrid rectification methods are consistently lower than those predicted by the model. This

is due to the assumption that the the magnetic interactions were negligible in this work. However, the permanent magnet on the tip mass could interact with the ferromagnetic leads in the reed switches or even any surrounding ferromagnetic metals. Incorporating these effects in a theoretical model is a daunting task due to the methods available for modeling magnetic field behavior and forces. However the possible effects of these forces should be explored to more fully determine the sources of power dissipation for both the reed switch and hybrid rectification methods.

2.6 Discussion

The results of the presented reed switch and hybrid rectification models allow for the informed design of effective low-loss, low-voltage systems. To create a theoretical model of the reed switch and hybrid rectification methods which captures more of the behavior requires the incorporation of multiple complex phenomenon, as mentioned in section 2.5.3. Future work should also include an accurate piezoelectric model accounting for electromechanical back-coupling effects from the electrical load. These effects were negligible in the presented work due to the measurement of the rectifier output at open circuit conditions.

Also, the experimental setup used to verify the expected behavior of the system was excited off-resonance to allow for more predictable tip deflection behavior. However, typical vibration energy harvester designs investigate resonant or broadband excitation. One method for accommodating the significant frequency-dependence of a vibration energy harvester's response is to place an array of switches parallel to the path of the tip mass, as opposed to just beyond

the extremes. Figure 2.16 illustrates the proposed configuration. This arrangement would allow for the actuation of pairs of switches at deflections less than the maximum amplitude. It should be noted that a minimum amount of separation should exist between SW_{P1} and SW_{P2} to prevent shorting the rectifier. As a result, while the proximity delay can be decreased using this method, one must always be present to prevent failure.

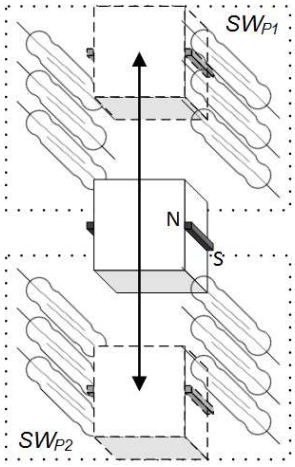

Figure 2.16: A mechanical schematic of the use of an array of reed switches parallel to the path of the tip mass for improved frequency-dependent behavior.

2.7 Conclusions

A low-loss hybrid AC-DC rectification technique is presented and evaluated to show higher performance levels than semiconductor diode full-bridge rectifiers. It utilizes a hybrid of mechanical switching by magnetically actuating reed switches and passive semiconductor diodes. Therefore, there is no power overhead requirement due to additional electronic components.

A theoretical model predicted the performance of the proposed rectification

scheme as compared to an offset diode model full-bridge rectifier. The hybrid rectification method's performance depends highly on the percentage of time during an oscillation half-period the switches are closed, dictated by the proximity delay and the hysteresis. Experiments performed below the resonance of the harvester showed a 6.8% increase in the output RMS voltage over a Schottky diode rectifier. A new configuration for the reed switches is also presented which would exhibit better broadband performance.

Lastly, although not examined in this work, both the reed switch and hybrid methods show potential for the rectification of low voltage harvesters. This is due to the small contact resistance of the reed switches and their operational dependence on the beam's tip deflection relative to the reed switch pull-in distance as opposed to the output voltage levels.

CHAPTER 3

SELF-RELIANT AVIAN BIO-LOGGER: ENERGY STORAGE CONSIDERATIONS

3.1 Introduction

As the capabilities of microcontroller (MCU) systems and communication electronics expand, the number and variety of feasible applications for low-power, low-mass embedded systems is drastically increasing. Particularly in the area of wireless sensor nodes for scientific studies. A key limitation for many new systems is the inability to provide adequate and robust energy. A robust energy supply is important as the system can take a greater frequency and a wider variety of measurements. Or put simply, more energy allows us to do more science.

Avian bio-logging and tracking is a highly desirable application [75, 56, 61, 62] which possesses very extreme design requirements as the bird needs to be able to fly unhindered. Multiple studies have been dedicated to setting a baseline for allowable payload on birds and the U.S. Geological Survey places a limit of 3-4% of the bird's body mass [26]; however, no consensus has yet to be reached in the literature [9, 10, 3]. Clearly, minimizing the payload intrusiveness by focusing on low volume and mass must remain a priority for the system design.

Avian migration studies are of particular interest with many topical reviews that mention the subject [8, 23, 6]. As migrations typically occur over the course of a year, these studies have long duration requirements, making a complex challenge even harder. The only reported systems with operational durations

long enough for a migration study are a 9 g geolocation logger [1], a 200 g GPS transmitter [43], and the 12 g solar-powered UvA-BiTS GPS tracking tag and acceleration bio-logger [5]. The 9 g geolocation logger lasts 8 years, but must be recaptured as it cannot upload the data remotely. The 200 g GPS transmitter lasts 300 days, but it is not designed to store large amounts of data and transmits the locations to nearby base stations frequency. The 12 g UvA-BiTS GPS tracking tag and acceleration bio-logger can theoretically operate indefinitely due to the onboard solar panels and battery. However, as with the other tracking tags, it's relatively large mass severely limits the number of bird species which can carry it. Coupled with the high demand for this capability in a device, it is clear technological limitations remain.

A couple of methods for decreasing the mass and increasing the capabilities of tracking tags and bio-loggers have been pursued by researchers in the literature. The use of solar energy harvesters on tracking tags has been in practice since 1973 [52]. Recharging batteries reduces the necessary energy storage as it no longer has to start out with all of the energy required over the duration of the study. These systems can achieve self-reliant operation as well, where the system either harvests more energy than required for operation or modulates its operation based on the level of stored energy. Multiple of these devices have been developed [5] and are even commercially available [66]. However, the characteristics of the energy storage still dictate the maximum operation load that the device can sustain for a set period of time. Another tactic is the combination of data logging functionality with wireless transmission, resulting in systems where catch-and-release is not necessary to obtain the data [70, 5]. These tags can also be deployed with smaller amounts of on-board memory. Decreasing the footprint of the memory increases the amount of payload which can be

devoted to energy considerations, allowing for longer duration deployments.

There are multiple types of commercial small-scale energy storage devices; however, they have very different performance characteristics. This makes meeting the energy and power requirements of wireless data communication and self-reliant operation a challenge. Figure 3.1 shows the specific energy and power information listed for a variety of commonly available small-scale energy storage devices (see appendix table A.1). Batteries have significantly higher specific energy levels than capacitors and super capacitors. The values for small-scale batteries shown in figure 3.1(a) are an order of magnitude lower than the $\sim$150 Wh/kg reported for lithium batteries due to a more significant portion of the overall mass being limited to packaging [59, 68]. However, many super capacitors have higher specific power levels and are commonly used for wireless data transmission tasks [64]. Surveyed super capacitors less than 1 gram did not show these advantages (figure 3.1(b)).

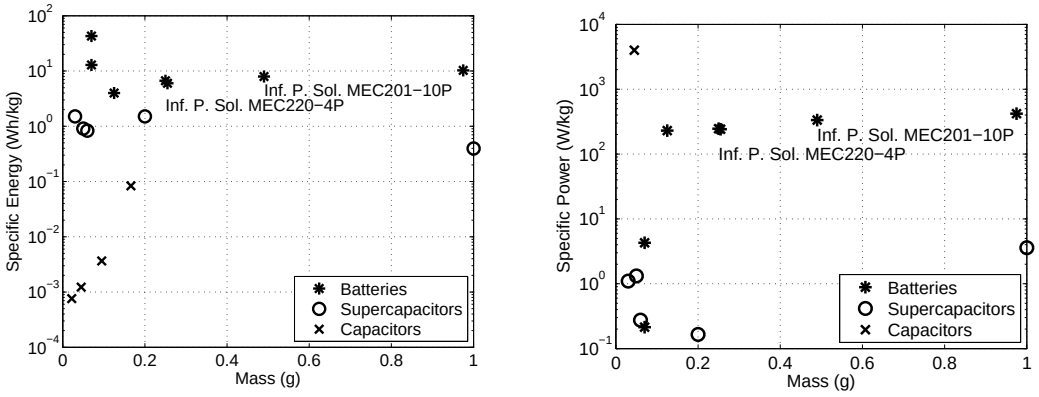

(a) (b)

Figure 3.1: The calculated (a) specific energy and (b) specific power specifications for commercially available small-scale energy storage devices.

As a result of the high specific power of super capacitors and the high specific energy of batteries, many researchers have explored a hybrid energy stor-

age approach [33, 30, 19]. These studies have looked at both passive and active configurations of batteries and super capacitors. The advantage of a hybrid system is the ability to provide higher instantaneous power levels than just batteries. They are used significantly for high-power pulse loads [30, 19]. However, Sikha *et al.* (2005) plotted the specific energy vs. the specific power, a Ragone plot, of hybrid systems against battery systems and concluded that battery systems are preferable for applications where minimal mass is a priority.

The purpose of this work is to address the energy storage considerations for a self-reliant avian bio-logger using small-scale lithium batteries. With a robust energy storage system, measurements can be taken more frequently to result in more data per study. The goal of our bio-logger is to monitor the subject's metabolism, transmit the data at points along the migration path, and have an overall system mass less than 4 g [56]. Multiple energy harvesting techniques are being explored to recharge the on-board energy storage mid-flight. Specifically harvesting the vibration energy from the flapping of the bird's wings and solar power [58, 62, 61]. Due to the expected mass of the energy harvesting transducers and the main system components, the battery must be less than 1 g. The energy and power requirements for the bio-logger are predicted by an overall system power and energy model. The primary design considerations for the energy storage are then explored experimentally. Lastly, a preliminary system is described which is able to provide high energy density storage for long durations and supply the power necessary for the bio-logger electronics, including the wireless communication. As a result, the capabilities of the proposed system increase the ability of scientists to perform remote, mass-restricted studies on wildlife *in situ*.

3.2 Bio-logger energy and power budget

To determine energy and power requirements for the bio-logger, an initial prototypical system was designed. The system is based on the ATmega128RFA1 microcontroller (MCU) with integrated 2.4 GHz RF communication. Although 2.4 GHz is inappropriate for the data communication of this application, it is used as a power requirement reference in this work due to the complexity involved in designing the specific communication system. The primary functionality of the proposed avian bio-logger is the measurement of the bird's uric acid levels to determine its metabolic rate. The uric acid sensor's periodic calibration lasts 15 minutes and each measurement requires 3 minutes. The sensor and its accompanying conditioning electronics require 81 μW [24]. Two other main components included in the power budget are the DS1337 serial real-time clock and the LTC4071 Li-ion/polymer battery charger. The real-time clock allows for longer-duration task scheduling and a more robust time-stamp than available solely with an MCU. The battery charger acts to protect the battery from over-charging and over-discharging. It limits the charging voltage to 4.1 V using an internal shunt regulator and completely isolates the battery from the load if its voltage drops to 2.7 V. This is advantageous because the battery charger consumes less power than the MCU active state and allows the MCU sleep state to be a larger portion of the duty cycle.

3.2.1 Energy and power requirements

Table 3.1 lists the reported power requirements for the bio-logger components. While the MCU and uric acid sensor are operating at a regulated 3.0 V, the real-

time clock and the battery charger are connected directly to the battery. This was done for the real-time clock so that complete loss of power from the regulated 3.0 V supply for the MCU does not result in a loss of timekeeping for the system. For the power requirements, both were assumed to use the maximum 4.1 V seen from the examined batteries. More details on the specific batteries will be discussed in section 3.3.1.

Table 3.1: Component power requirements for the bio-logger.

Component	**State**	**Voltage (V)**	**Current (mA)**
ATmega128RFA1	16 MHz Active	3.0	4.5
	Deep Sleep	3.0	2.5×10^{-4}
	TX	3.0	14.5
	RX	3.0	12.5
DS1337	Active	4.1	0.15
	Timekeeping	4.1	6×10^{-4}
LTC4071	Active	4.1	1.2×10^{-3}
Uric Acid Sensor	Active	3.0	8.1×10^{-2}

The expected power consumed during different modalities of behavior for the bio-logger can be calculated. These modalities are: the MCU active state, the system sleep state, wireless data transmission (TX) and receiving (RX), and sensing. When the system is in its active state, the MCU draws approximately 4.5 mA. The real-time clock would also be in its active state to communicate with the MCU. This adds 0.15 mA along with the battery charger's 1.2 μA to the current draw. As a result, the active state requires 14 mW. Using the same reasoning, the system's sleep state draws 8.13 μW, wireless transmission draws 43.5 mW, and receiving draws 37.5 mW. For the uric acid sensor, the MCU does not need to be in the active state except at the very beginning and end of the operation. Therefore when the uric acid sensor is operating the system draws 89 μW.

Based on the power consumption of the different modalities, energy requirements can be determined for different system tasks. These tasks are: wireless data upload, pinging to attempt to locate a base station, calibrating the uric acid sensor, taking a measurement, saving the measurement, sleeping between measurements, and checking the state-of-charge (SOC) of the battery. Multiple parameters need to be determined to calculate an estimate for the amount of energy required to upload the saved data to a base station. First, the standard 802.15.4 transmission rate of 250 kbit/s is assumed. At this rate it would require 8 sec to transmit 256 kByte worth of memory. The amount of memory required depends on multiple factors as well, but the 256 kByte M24M02-DR is available in very small SO78N and WLCSP packages and is used for these calculations. This can be thought of as the case where only very infrequent data uploads are possible. A conservative estimate is 10 sec for the transmission to account for any additional protocols, resulting in approximately 435 mJ. For a 4.1 V battery, this is $\approx$29 μAh. A ping is the system sending out a short transmission and then listening for a response. In this instance we will assume both actions take 2 seconds to allow for multiple attempts in succession, resulting in approximately 160 mJ. For a 4.1 V battery, this is $\approx$11 μAh. As mentioned previously, the uric acid sensor calibration test lasts 15 minutes and the measurement lasts 3 minutes. Each calibration requires 80 mJ and each measurement requires 16 mJ, translating into $\approx$5.4 μAh and $\approx$1.1 μAh for a 4.1 V battery. Once the measurement has been taken, the system needs to save it to the memory. The amount of time this task takes depends on multiple factors and is assumed to be 1 second. This corresponds to 14 mJ of energy and $\approx$1 mAh on the battery. Between the measurement tasks the system is in its sleep mode. If we assume the system is not asleep for more than an hour at a time, it will require less than 30 mJ, or $\approx$2

μAh.

The last system task is checking the SOC of the battery. For this task, the system will wake up, check the battery SOC with a voltage measurement, update the state flags, and go back to sleep. State flags refer to logic bits telling the MCU what state it is in when it wakes up from a sleep mode. Using the ATmega128RFA1 datasheet, a maximum of 300 μsec for a voltage measurement can be expected. As multiple factors dictate the time required to update the state flags in the memory, it is lumped into a conservative estimate of 1 msec for each time. Therefore the system consumes 14 μJ of energy each time, or $\approx$1 nAh.

3.2.2 Operating scenario

To determine the energy requirements which need to be supplied by the energy storage system, the amount of energy consumed by the system over the course of a typical day of migration activity is calculated. Assume during normal operation the system calibrates the uric acid sensor once. It then makes a uric acid sensor measurement and sends out a ping every hour. Also assume the system is otherwise active for a total of 1 second each hour to perform all of the necessary activities, such as measuring the battery SOC and saving data. The uric acid sensor calibration consumes approximately 80 mJ. Each hour the system consumes approximately 220 mJ, including the time spent in the sleep mode. As a result, over the course of the day the system consumes 5.36 J. For a 4.1 V battery this corresponds to 363 μAh. Depending on the complexity of the embedded software on the bio-logger, other scenarios can be taken into account as well. For example, the behavior of the system while the bird is nesting or when

the system detects a low SOC and goes into a separate “low-battery” mode.

3.3 Energy storage system design

The design of the energy storage for the bio-logger is paramount for the robust operation of the system. Loss of power for significant periods of time or damage to the battery results in large data gaps or no data at all. Careful consideration must be given to the various nonlinear behaviors the batteries exhibit.

3.3.1 Proposed battery systems

For this work, two MEC220-4P’s connected in a passive parallel configuration and a single MEC201-10P were examined (table 3.2). It should be noted that the two batteries in parallel have an equivalent capacity of 800 μAh as compared to the 1 mAh for the single battery. Placing batteries in parallel configurations has been explored in the literature using valve-regulated lead acid (VRLA) batteries. A passive parallel configuration is a method for combining the output of multiple cells which requires minimal additional conditioning circuitry [45, 15]. The advantage of using multiple smaller batteries comes from the adaptability. Due to the small thickness of the cells, the difference in the amount of space 2 or more batteries takes up compared to a single one is minimal. As a result, a single system can be designed for a range of bird species and maximum payload sizes. For example, with the MEC220-4P’s the batteries can be placed in a slot that is 25.4 x 12.7 x 1 mm. For the smallest birds, the minimum necessary number of cells can be used and the bio-logger behavior programmed accord-

ingly. However, for larger birds which can carry more mass, additional cells of the same model can easily be added to increase the energy storage. By having more energy storage capacity, the bio-logger can be programmed to take measurements much more frequently, resulting in more data and more informative studies. These models were chosen due to their high specific power compared to the other batteries surveyed (figure 3.1).

Table 3.2: Specifications of the Infinite Power Solutions MEC220-4P and MEC201-10P lithium batteries.

Specification	**MEC220-4P**	**MEC201-10P**
$V_{OC}(V)$	4.1	4.1
Dimensions (mm)	25.4 x 12.7 x 0.17	25.4 x 25.4 x 0.17
Mass (g)	0.255	0.490
$R_{Int.}(\Omega)$	100	35
$I_{max}(mA)$	15	40
Capacity (mAh)	0.4	1.0
Cycles	100,000	100,000
Spec. Power (W/kg)	241	335
Spec. Energy (Wh/kg)	6	8

3.3.2 Experimental characterization

Experiments were performed to verify the manufacturer-provided specifications and the expected performance for the two MEC220-4P's in parallel. The experimentally observed non-linear behavior can then be used to design a more robust system. The batteries were charged and discharged in conjunction with the LTC4071 battery charger (figure 3.2).

Figure 3.3 shows the results of the discharge experiments. The curves start from the fully charged state at 4.1 V and end when the LTC4071 disconnects the

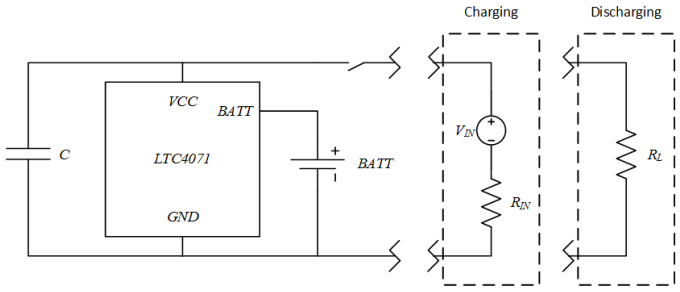

Figure 3.2: Experimental setup for battery charging and discharging using the LTC4071 battery charger.

battery at 2.7 V, above the 2.1 V minimum specified by the manufacturer. The SOC is defined as the remaining energy stored on the battery normalized by the total capacity. The initial voltage drop shown in figures 3.3(a) and 3.3(b) is due to the internal resistance of the batteries. The two MEC220-4P batteries in parallel perform very similarly to the single MEC201-10P with the exception of the expected differences due to the different capacities.

The experimental operation time, final SOC, specific power, and specific energy were calculated for each test (figure 3.4). Figure 3.4(a) shows that both systems are able to provide an average power greater than 50 mW for more than 40 sec from the fully-charged state. As a result these tests confirm the ability of the batteries to perform the 10 second, 43 mW data communication estimate calculated earlier. However, these experiments showed that the battery coupled with the LTC4071 produced specific power levels significantly below the manufacturer-provided values (figure 3.4(c) and table 3.2). Attempts to extract more power from the batteries caused the LTC4071 to immediately isolate the battery as the initial loaded voltage dropped to 2.7 V.

Figure 3.4(d) shows that the experimental specific energies are very close to the manufacturer-provided specifications at low loads (table 3.2). When the

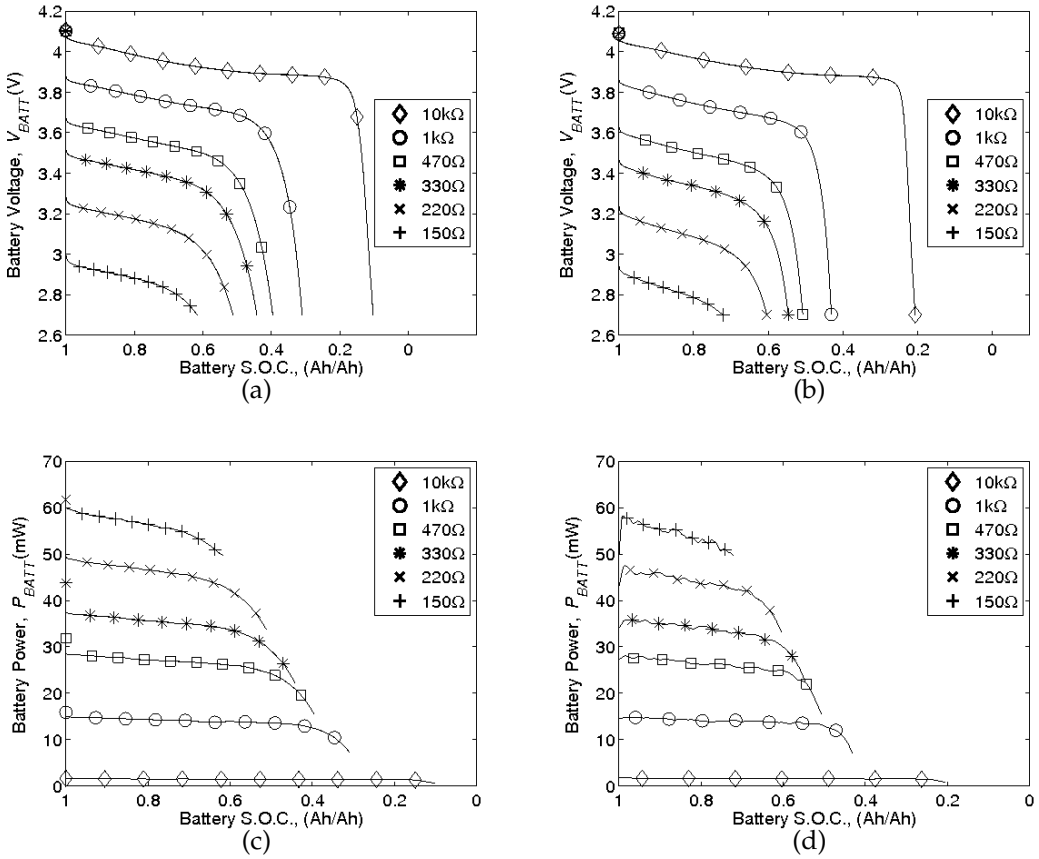

Figure 3.3: Experimental battery discharge curves for the (a & c) the MEC201-10P and (b & d)the two MEC220-4P's with $C = 0$.

load increases, the specific energy decreases. This is explained by the final SOC values in figure 3.4(b), which increase as the average power increases. This behavior can also be seen in figures 3.3(a) and 3.3(b), which show the battery voltage dropping to 2.7 V earlier in its discharge as the load resistance decreases. For a robust bio-logger energy system, the trends in specific energy and power must be taken into consideration when determining the necessary capacity.

Another factor which must be taken into account is the variability of the practical battery specifications, mainly the internal impedance. This starts with the inherent inconsistency of manufacturing lithium batteries and continues as individual cells experience different loads or operating conditions. How-

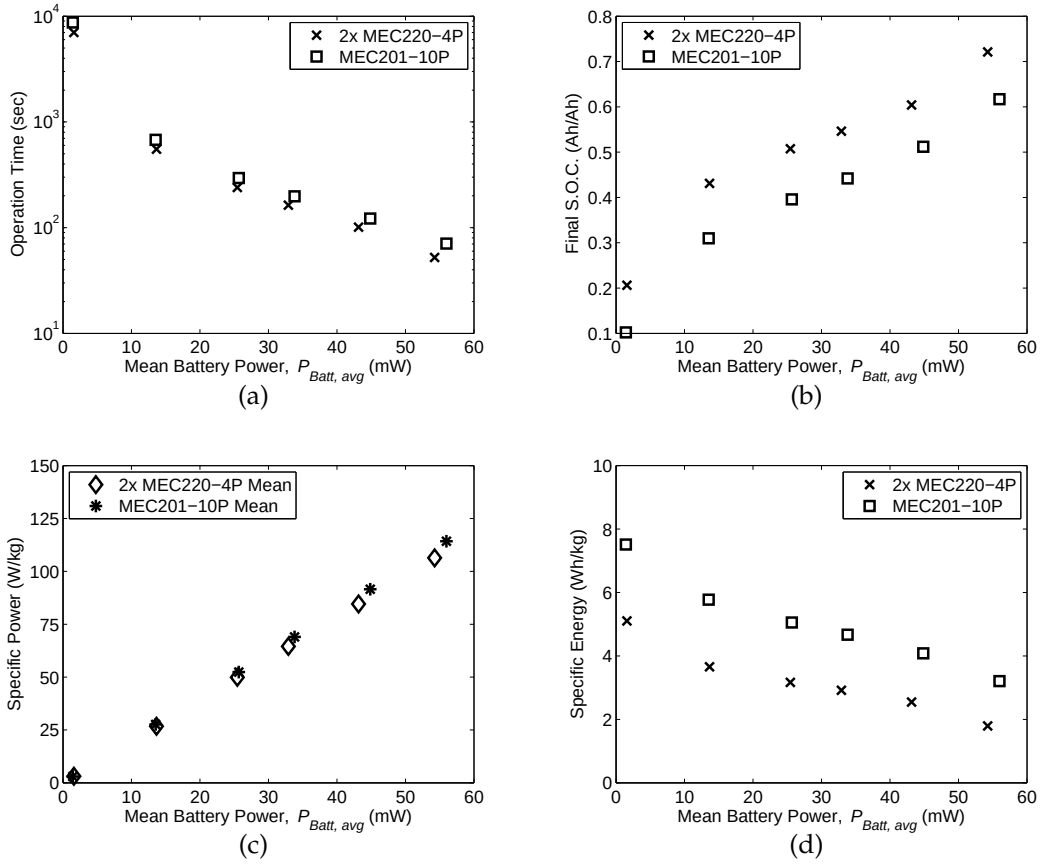

Figure 3.4: Performance comparisons of the two MEC220-4P's in parallel and the MEC201-10P battery for the (a) operation time, (b) final SOC, (c) specific power, and (d) specific energy.

ever, experiments were performed to show that the same behavior exhibited by VRLA batteries can be expected for the examined lithium batteries as well (figure 3.5).

The 10 kΩ charging case is not shown because the charge current is limited to 0.41 mA by the input resistor and therefore for that test the result does not illustrate the behavior of the batteries themselves. The individual MEC220-4P marked by the dashed gray line provides more power during discharging tests and draws more power during charging tests. The consistency verifies the expected behavior that the system automatically adjusts the load distribution

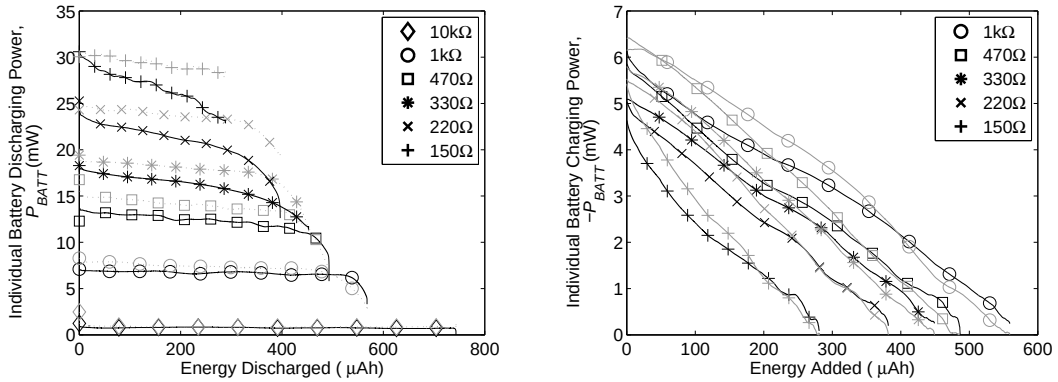

(a) (b)

Figure 3.5: Power outputs from individual batteries (solid black vs. dashed gray) during (a) discharging and (b) charging experiments for the two MEC220-4P's in parallel.

according to the relative impedances of the two cells.

3.3.3 System load performance

To validate the ability of the energy storage systems to meet the extreme load demands of the bio-logger, a Keithley 2400 Sourcemeter controlled through an RS-232 interface using the MATLAB software package emulated a prototypical wireless communication and data transmission load profile. Figure 3.6(a) shows the load profile used. It has five pings and on the fifth, it is answered. That results in a "handshake" to initiate the connection, another combination of TX and RX tasks. The data is then transmitted over the course of 10 seconds. Lastly, another "handshake" is performed to indicate the end of the data transmission. All of the load values for the modalities are based on the calculated power estimates from section 3.2.1.Both the two MEC220-4P's in parallel and the MEC201-10P battery (not shown) are able to provide the necessary power profile required to complete the prototypical wireless communication and data

transmission.

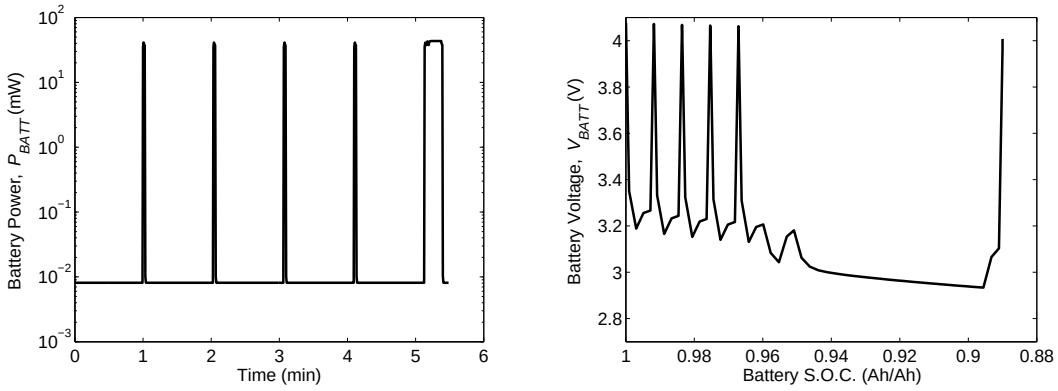

(a) (b)

Figure 3.6: Experimental performance of the two MEC220-4P's in parallel with a prototypical wireless communication and data transmission profile.

3.4 Preliminary system design

Using the presented energy and power budgets in conjunction with the experimentally obtained data on the performance of the batteries, a preliminary system can be designed. The MCU, real-time clock, and battery charger have already been chosen and discussed. This section will focus on finalizing the energy storage and harvesting devices for the system.

3.4.1 Energy storage system

As mentioned in section 3.3.2, the portion of the battery capacity available for an operation is directly related to the load level. Therefore, to determine the actual overall battery capacity needed for the bio-logger, the power and energy

budgets for the major system tasks are compared to the battery experimental performance.

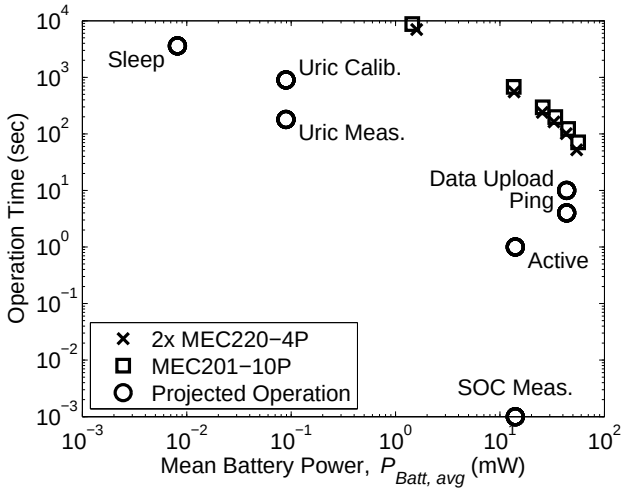

Figure 3.7: The projected necessary operation times for the system energy and power model compared with the battery system experimental performance.

Figure 3.7 shows the projected requirements for operation time and battery capacity of the system tasks defined in section 3.2.1. These were the wireless data upload, the wireless ping, calibrating the uric acid sensor, taking a uric acid measurement, measuring the SOC of the battery, saving the data into memory, and putting the system in sleep mode between operations. The plots also have the experimental performance obtained for the batteries in section 3.3.2. For both the operation time and necessary battery energy, the major design limitation comes from the wireless data communication activities, the two data points at 43 mW.

Recall that both the two MEC220-4P's in parallel and the single MEC201-10P were experimentally shown to provide up to 60 mW. A survey of energy storage devices (figure 3.1) showed that these batteries possessed the highest spe-

cific power for the lithium batteries examined. As a result, the required energy capacity cannot be easily decreased. Using only one MEC220-4P to halve the mass would result in only being able to supply 30 mW of power, less than that needed for wireless communication. Therefore, the two MEC220-4P's in parallel or the single MEC201-10P represent good baseline energy storage systems for the bio-logger.

3.4.2 Energy harvesting estimates

An important aspect for a self-reliant system is energy neutral operation, i.e. when the energy expended through normal use is equal to or less than the harvested energy. Previously, we described a normal daily operational scenario requiring 5.36 J. However, it must be determined if this is a realistic amount of energy for the solar and vibration energy harvesters to produce.

Using the 4 g goal and a 3-4% of body mass limit, the smallest bird the tag can be attached to is 133 g. Shafer *et al.* (2012) report that for a bird of that size, there is 0.5 - 1 mW of harvestable power for a 0.1 - 0.3 W/kg device. If we assume the piezoelectric harvester is no more than 25% of the bio-logger's mass at 1 g, then we can expect at least 0.125 mW of harvested power. At this production level, it would require 12 hours of active flight to achieve energy neutral operation. For the photovoltaic harvester, the Spectrolabs TASC provides up to 30% efficiency in a thin package, or 27 mW/cm^2. For a one square centimeter ($\sim$103 mg) photovoltaic cell it would take only 3.3 min of maximum power output for energy neutral operation. With the combination of the two harvesting methods, these estimates illustrate that the primary factor which will limit the

capabilities of the bio-logger is the ability to provide the power necessary for the data upload and that energy neutral operation for the described daily behavior is achievable.

3.4.3 System scalability

One of the advantages of using multiple batteries in parallel as opposed to a single larger unit is the adaptability of the energy storage. As the specific power and energy levels dictate the amount of data which can be uploaded from the bio-logger at one time, having a larger battery would allow for more data to be transmitted. Or put simply, more batteries in parallel allow us to do more science. This is limited by the remaining payload available for the species of bird that is involved in the study. With the 2 MEC220-4P's at 255 mg each, the 103 mg solar cell, and the 1 g piezoelectric harvester, the major sources of mass for the system combine to only 1.6 g. This leaves 2.3 g for the circuit components, the packaging, and the method to attach the device to the bird. If the bird can carry more than 4 g or the remaining items don't combined to 2.3 g, more batteries can be used. By placing three or more of the MEC220-4P's in parallel on the bio-logger more than 256 kBytes of data can be transmitted at one time. This would allow for more frequent uric acid sensor measurements, less frequent data uploads, and even more different sensor measurements such as location, temperature, or barometric pressure.

3.5 Conclusions

This work addresses the challenge of supplying power and storing energy for a self-reliant avian bio-logger aimed at measuring uric acid levels for long-term migration studies. Due to the limited payloads bird's can carry without hindering their flight, the mass and volume of the energy storage system must be small to encompass as many species of birds as possible. The system must also be able to wireless upload saved data periodically.

A preliminary system is designed and power requirements calculated for a scenario which included different operation modalities and system tasks. The necessary stored energy to perform the tasks, such taking a uric acid sensor measurement or uploading the saved data, is then determined. Using these design parameters and the experimental characterization of small-scale, thin-film lithium batteries a baseline energy storage system is proposed. Also, the amount of harvested energy using both piezoelectric and photovoltaic harvesters is predicted to show that sufficient levels can be produced to allow for energy neutral operation during active migration flight.

The main limiting factor was determined to be the battery's ability to provide the necessary power for wireless communication. While the batteries chosen for this study showed the highest specific power levels of the small-scale devices surveyed, their ability to be placed in a passive parallel configuration allows for increasing the maximum power and energy storage levels as high as the mass limits allow. By doing so, more data can be transmitted at any given time. This allows for either more sensors, more frequent measurements, or less frequent data upload events.

APPENDIX A

LIST OF REFERENCED COMMERCIAL COMPONENTS FOR CHAPTER 3

Table A.1: The energy storage devices listed in figure 3.1.

Manufacturer	**Model Number**
Super Capacitors	
AVX	BZ013B503ZSB
AVX	BZ013A703ZSB
AVX	BZ113B104ZSB
Panasonic	EEC-RG0V105
Panasonic	EEC-RG0V224
Panasonic	EEC-EN0F204J2
Panasonic	EEC-EP0F333Y
Taiyo Yuden	PAS311HR-VA6R
Taiyo Yuden	PAS409HR-VE5R
Batteries	
Infinite Power Solutions	MEC225-1P
Infinite Power Solutions	MEC220-4P
Infinite Power Solutions	MEC120-4P
Infinite Power Solutions	MEC201-10P
Infinite Power Solutions	MEC202-25P
Seiko	MS412FE
Seiko	HB414
Capacitors	
Panasonic	ECJ-4YB1H105K
Panasonic	ECJ-3VB1C474K
Taiyo Yuden	JMK316B7106KL-T
AVX	SR151C103KAR

Table A.2: The off-the-shelf bio-logger components.

Device	**Manufacturer**	**Model Number**
Microcontroller	ATMEL	ATmega128RFA1
Serial Real-Time Clock	MAXIM	DS1337
Li-Ion/Polymer Battery Charger	Linear Technology	LTC4071

BIBLIOGRAPHY

[1] V Afanasyev. A miniature daylight level and activity data recorder for tracking animals over long periods. *Memoirs of National Institute of Polar Research*, 58:227–233, 2004.

[2] S R Anton and H A Sodano. A review of power harvesting using piezoelectric materials (2003-2006). *Smart Materials and Structures*, 16(3):R1–R21, June 2007.

[3] D G Barron, J D Brawn, and P J Weatherhead. Meta–analysis of transmitter effects on avian behaviour and ecology. *Methods in Ecology and Evolution*, 1(2):180–187, February 2010.

[4] B S Borowy and Z M Salameh. Optimum photovoltaic array size for a hybrid wind/PV system. *IEEE Transactions on Energy Conversion*, 9(3):482–488, 1994.

[5] W Bouten, E W Baaij, J Shamoun-Baranes, and K C J Camphuysen. A flexible GPS tracking system for studying bird behaviour at multiple scales. *Journal of Ornithology*, 154:571–580, November 2013.

[6] E S Bridge, K Thorup, M S Bowlin, P B Chilson, R H Diehl, R W Fléron, P Hartl, R Kays, J F Kelly, W D Robinson, and M Wikelski. Technology on the Move: Recent and Forthcoming Innovations for Tracking Migratory Birds. *BioScience*, 61(9):689–698, September 2011.

[7] M Bryant and E Garcia. Modeling and Testing of a Novel Aeroelastic Flutter Energy Harvester. *Journal of Vibration and Acoustics*, 133(1.011010):1–11, 2011.

[8] A E Burger and S A Shaffer. Application of Tracking and Data–Logging Technology in Research and Conservation of Seabirds. *The Auk*, 125(2):253–264, April 2008.

[9] D F Caccamise and R S Hedin. An aerodynamic basis for selecting transmitter loads in birds. *The Willson Bulletin*, 97(3):306–318, 1985.

[10] B Calvo and R W Furness. A review of the use and the effects of marks and devices on birds. *Ringing and Migration*, 13:129–151, 1992.

[11] L Chao, C Y Tsui, and W H Ki. Vibration energy scavenging and management for ultra low power applications. In *Iternational symposium on Low power electronics and design*, pages 316–321, 2007.

[12] P L Chapman. Power management for energy harvesting devices. In *IEEE Radio and Wireless Symposium*, pages 9–12, January 2009.

[13] S Cheng, Y Jin, Y Rao, and D P Arnold. An Active Voltage Doubling AC / DC Converter for Low-Voltage Energy Harvesting Applications. *IEEE Trans. on Power Electronics*, 26(8):2258–2265, 2011.

[14] S Cheng, R Sathe, R D Natarajan, and D P Arnold. A Voltage–Multiplying Self–Powered AC / DC Converter with 0 . 35–V Minimum Input Voltage for Energy Harvesting Applications. *IEEE Transactions on Power Electronics*, 26(9):2542–2549, 2011.

[15] B A Cole, R J Schmitt, and J Szymborski. Operational Characteristics of VRLA Batteries Configured in Parallel Strings. In *Telecommunications Energy Conference*, pages 356–363, 1998.

[16] E Dallago, G Frattini, D Miatton, G Ricotti, and G Venchi. Integrable High–Efficiency AC–DC Converter for Piezoelectric Energy Scavenging System. In *IEEE International Conference on Portable Information Devices*, pages 1–5, May 2007.

[17] M K Deshmukh and S S Deshmukh. Modeling of hybrid renewable energy systems. *Renewable and Sustainable Energy Reviews*, 12(1):235–249, January 2008.

[18] J M Dietl and E Garcia. Beam Shape Optimization for Power Harvesting. *Journal of Intelligent Material Systems and Structures*, 21(6):633–646, March 2010.

[19] R A Dougal, S Liu, and R E White. Power and Life Extension of Battery - Ultracapacitor Hybrids. *IEEE Transactions on Components and Packaging Technologies*, 25(1):120–131, 2002.

[20] R Dufo-López and J L Bernal-Agustín. Design and control strategies of PV–Diesel systems using genetic algorithms. *Solar Energy*, 79(1):33–46, July 2005.

[21] S Dwari and L Parsa. An Efficient AC - DC Step–Up Converter for

Low–Voltage Energy Harvesting. *IEEE Transactions on Power Electronics*, 25(8):2188–2199, 2010.

[22] N G Elvin and A A Elvin. A General Equivalent Circuit Model for Piezoelectric Generators. *Journal of Intelligent Material Systems and Structures*, 20(1):3–9, May 2009.

[23] W Fiedler. New technologies for monitoring bird migration and behaviour. *Ringing and Migration*, 24(3):175–179, 2011.

[24] A Gumus, D Winkler, and D Erickson. Lab on a bird: autonomous microsystems for in–vivo real time biophysical monitoring of birds. In *International Conference on Miniaturized Systems for Chemistry and Life Sciences*, pages 2004–2006, 2011.

[25] S Guo and H Lee. An Efficiency–Enhanced Integrated CMOS Rectifier with Comparator–Controlled Switches for Transcutaneous Powered Implants. In *IEEE Custom Integrated Circuits Conference*, pages 385–388, 2007.

[26] M E Gustafson, J Hildenbrand, and L Metras. The North American Bird Banding Manual, 1997. Accessed May 2013.

[27] D Guyomar, A Badel, E Lefeuvre, and C Richard. Toward energy harvesting using active materials and conversion improvement by nonlinear processing. *IEEE Transactions on Ultrasonics, Ferrorelectrics, and Frequency Control*, 52(4):584–595, 2005.

[28] D Guyomar, Y Jayet, L Petit, E Lefeuvre, T Monnier, and C Richard. Synchronized switch harvesting applied to selfpowered smart systems : Piezoactive microgenerators for autonomous wireless transmitters. *Sensors and Actuators A*, 138:151–160, 2007.

[29] Hamlin. AN104: Reed Switch and Reed Sensor Activation. Technical report, 2008.

[30] C E Holland, J W Weidner, R A Dougal, and R E White. Experimental characterization of hybrid power systems under pulse current loads. *Journal of Power Sources*, 109(1):32–37, June 2002.

[31] A Kansal, J Hsu, S Zahedi, and M B Srivastava. Power management in energy harvesting sensor networks. *ACM Transactions on Embedded Computing Systems*, 6(4):32–es, September 2007.

[32] N Kong, D S Ha, A Erturk, and D J Inman. Resistive Impedance Matching Circuit for Piezoelectric Energy Harvesting. *Journal of Intelligent Material Systems and Structures*, 21(13):1293–1302, January 2010.

[33] A Kuperman and I Aharon. Battery-ultracapacitor hybrids for pulsed current loads: A review. *Renewable and Sustainable Energy Reviews*, 15(2):981–992, February 2011.

[34] M Lallart and D Guyomar. An optimized self–powered switching circuit for non–linear energy harvesting with low voltage output. *Smart Materials and Structures*, 17(035030):1–8, June 2008.

[35] T T Le, J Han, A V Jouanne, K Mayaram, and T S Fiez. Piezoelectric Micro-Power Generation Interface Circuits. *IEEE Journal of Solid-State Circuits*, 41(6):1411–1420, 2006.

[36] E Lefeuvre, D Audigier, C Richard, and D Guyomar. Buck–Boost Converter for Sensorless Power Optimization of Piezoelectric Energy Harvester. *IEEE Transactions on Power Electronics*, 22(5):2018–2025, September 2007.

[37] E Lefeuvre, A Badel, A Benayad, L Lebrun, C Richard, and D Guyomar. A comparison between several approaches of piezoelectric energy harvesting. *J. Physics IV in France*, 128:177–186, 2005.

[38] E Lefeuvre, A Badel, C Richard, and D Guyomar. Piezoelectric energy harvesting device optimization by synchronous electric charge extraction. *Journal of Intelligent Material Systems and Structures*, 16:865–876, 2005.

[39] H Lhermet, C Condemine, M Plissonnier, R Salot, P Audebert, and M Rosset. Efficient Power Management Circuit: From Thermal Energy Harvesting to Above–IC Microbattery Energy Storage. *IEEE Journal of Solid-State Circuits*, 43(1):246–255, January 2008.

[40] R MacCurdy, T Reissman, E Garcia, and D Winkler. A Methodology for Applying Energy Harvesting to Extend Wildlife Tag Lifetime. In *ASME International Mechanical Engineering Congress and Exposition*, pages 121–130, 2008.

[41] T Markvart. Sizing of hybrid photovoltaic–wind energy systems. *Solar Energy*, 57(4):277–281, 1996.

[42] M Marzencki, Y Ammar, and S Basrour. Integrated power harvesting sys-

tem including a MEMS generator and a power management circuit. *Sensors and Actuators A: Physical*, 145-146:363–370, July 2008.

[43] K Mase, T Kajita, and Y Zhang. A wide–area bird monitoring system using geographically distributed base stations. In *IEEE Wireless Communications and Networking Conference*, pages 2059–2064, March 2011.

[44] P D Mitcheson, T C Green, and E M Yeatman. Power processing circuits for electromagnetic, electrostatic and piezoelectric inertial energy scavengers. *Microsystem Technologies*, 13(11–12):1629–1635, January 2007.

[45] C S Moo, K S Ng, and Y C Hsieh. Parallel Operation of Battery Power Modules. *IEEE Transactions on Energy Conversion*, 23(2):701–707, 2008.

[46] R Morais, S G Matos, M A Fernandes, A L G Valente, S F S P Soares, P J S G Ferreira, and M J C S Reis. Sun, wind and water flow as energy supply for small stationary data acquisition platforms. *Computers and Electronics in Agriculture*, 64(2):120–132, December 2008.

[47] C Moser, L Thiele, D Brunelli, and L Benini. Adaptive Power Management in Energy Harvesting Systems. In *Design, Automation and Test in Europe Conference and Exhibition*, pages 1–6, April 2007.

[48] G K Ottman, H F Hofmann, A C Bhatt, and G A Lesieutre. Adaptive piezoelectric energy harvesting circuit for wireless remote power supply. *IEEE Transactions on Power Electronics*, 17(5):669–676, September 2002.

[49] C Park and P Chou. AmbiMax: Autonomous Energy Harvesting Platform for Multi–Supply Wireless Sensor Nodes. In *IEEE Communications Society on Sensor and Ad Hoc Communications and Networks*, pages 168–177, 2006.

[50] C H Park. On the Circuit Model of Piezoceramics. *Journal of Intelligent Materials Systems and Structures*, 12(7):515–522, July 2001.

[51] G Park, T Rosing, M D Todd, C R Farrar, and W Hodgkiss. Energy Harvesting for Structural Health Monitoring Sensor Networks. *Journal of Infrastructure Systems*, 14(1):64–79, March 2008.

[52] D R Patton, D W Beaty, and R H Smith. Solar Panels: An Energy Source for Radio Transmitters on Wildlife. *Journal of Wildlife Management*, 37(2):236–238, 1973.

[53] C Peters, J Handwerker, D Maurath, and Y Manoli. An ultra–low–voltage active rectifier for energy harvesting applications. In *IEEE International Symposium on Circuits and Systems*, pages 889–892, May 2010.

[54] C Peters, D Spreemann, M Ortmanns, and Y Manoli. A CMOS integrated voltage and power efficient AC/DC converter for energy harvesting applications. *Journal of Micromechanics and Microengineering*, 18(10):104005, October 2008.

[55] A Schlichting, E Fink, and E Garcia. A low-loss hybrid rectification technique for piezoelectric energy harvesting. *Smart Materials and Structures*, 2013. In Press.

[56] A Schlichting, M W Shafer, and E Garcia. Multi–source energy harvesting schemes with piezoelectrics and photovoltaics on an avian bio–logger. In *ASME Conference on Smart Materials, Adaptive Structures and Intelligent Systems*, pages 1–9, 2012.

[57] A Schlichting, R Tiwari, and E Garcia. Passive multi–source energy harvesting schemes. *Journal of Intelligent Material Systems and Structures*, August 2012.

[58] A Schlichting, R Tiwari, and E Garcia. Passive multi–source energy harvesting schemes. *Journal of Intelligent Material Systems and Structures*, 23(17):1921–1935, August 2012.

[59] B Scrosati and J Garche. Lithium batteries: Status, prospects and future. *Journal of Power Sources*, 195(9):2419–2430, May 2010.

[60] Helmut Sennewald. Solar cell model. `http://tech.groups.yahoo.com/group/LTspice/files/%20Lib/Solar%20Cell%20Module/`, 2007. Date Accessed: August 2011.

[61] M W Shafer, M Bryant, and E Garcia. A practical power maximization design guide for piezoelectric energy harvesters inspired by avian bio–loggers. In *ASME Conference on Smart Materials, Adaptive Structures and Intelligent Systems*, pages 1–10, 2012.

[62] M W Shafer, R MacCurdy, E Garcia, and D Winkler. Harvestable vibrational energy from an avian source: theoretical predictions vs. measured values. In *SPIE Vol. 8341*, pages 1–7, 2012.

[63] Y C Shu, I C Lien, and W J Wu. An improved analysis of the SSHI interface in piezoelectric energy harvesting. *Smart Materials and Structures*, 16(6):2253–2264, December 2007.

[64] F I Simjee and P H Chou. Efficient Charging of Supercapacitors for Extended Lifetime of Wireless Sensor Nodes. *IEEE Transactions on Power Electronics*, 23(3):1526–1536, May 2008.

[65] H A Sodano, D J Inman, and G Park. A Review of Power Harvesting from Vibration Using Piezoelectric Materials. *The Shock and Vibration Digest*, 36(3):197–205, May 2004.

[66] Telemetry Solutions. Quantum 4000 FL GPS Backpack Series. Technical report, 2013. Accessed on–line, Aug. 2013.

[67] S M Sze. *Physics of Semiconductor Devices*. Wiley-Interscience, USA, 2nd ed. edition, 1981.

[68] M M Thackeray, C Wolverton, and E D Isaacs. Electrical energy storage for transportation - approaching the limits of, and going beyond, lithium–ion batteries. *Energy and Environmental Science*, 5(7):7854, 2012.

[69] R Tiwari, K Ryoo, A Schlichting, and E Garcia. Extremely low–loss rectification methodology for low–power vibration energy harvesters. *Smart Materials and Structures*, 22(6):1–8, June 2013.

[70] S M Tomkiewicz, M R Fuller, J G Kie, and K K Bates. Global positioning system and associated technologies in animal behaviour and ecological research. *Philosophical transactions of the Royal Society of London. Series B, Biological sciences*, 365:2163–76, July 2010.

[71] F Valenciaga and P F Puleston. Supervisor Control for a Stand-Alone Hybrid Generation System Using Wind and Photovoltaic Energy. *IEEE Transactions on Energy Conversion*, 20(2):398–405, June 2005.

[72] B Wichert. PV–Diesel hybrid energy systems for remote area power generation – a review of current practice and future developments. *Renewable and Sustainable Energy Reviews*, 1(3):209–228, 1997.

[73] A Wickenheiser and E Garcia. Combined Power Harvesting from AC and DC Sources. In *SPIE Vol. 7288, Active and Passive Smart Structures and Integrated Systems*, pages 1–9, San Diego, CA, 2009.

[74] A M Wickenheiser and E Garcia. Power Optimization of Vibration Energy Harvesters Utilizing Passive and Active Circuits. *Journal of Intelligent Material Systems and Structures*, 21(13):1343–1361, July 2010.

[75] M Wikelski, R W Kays, N J Kasdin, K Thorup, J A Smith, and G W Swenson. Going wild: what a global small–animal tracking system could do for experimental biologists. *The Journal of experimental biology*, 210(Pt 2):181–6, January 2007.

[76] W J Wu, A M Wickenheiser, T Reissman, and E Garcia. Modeling and experimental verification of synchronized discharging techniques for boosting power harvesting from piezoelectric transducers. *Smart Materials and Structures*, 18(055012):1–14, May 2009.